10-20-2009

Optical and Terahertz Energy Concentration on the Nanoscale in Plasmonics

Anastasia Rusina
Georgia State University

OPTICAL AND TERAHERTZ ENERGY CONCENTRATION ON THE NANOSCALE IN PLASMONICS

by

ANASTASIA RUSINA

Under the Direction of Dr. Mark I. Stockman

ABSTRACT

We introduce an approach to implement full coherent control on nanometer length scales. It is based on spatiotemporal modulation of the surface plasmon polariton (SPP) fields at the thick edge of a nanowedge. The SPP wavepackets propagating toward the sharp edge of this nanowedge are compressed and adiabatically concentrated at a nanofocus, forming an ultrashort pulse of local fields. The profile of the focused waveform as a function of time and one spatial dimension is completely coherently controlled.

We establish the principal limits for the nanoconcentration of the terahertz (THz) radiation in metal/dielectric waveguides and determine their optimum shapes required for this nanoconcentration. We predict that the adiabatic compression of THz radiation from the initial spot size of vacuum wavelength $R_0 \approx \lambda_0 \approx 300\,\mu m$ to the unprecedented final size of $R = 100 - 250\,\text{nm}$ can be achieved, while the THz radiation intensity is increased by a factor of 10 to 250. This THz energy nanoconcentration will not only improve the spatial resolution and increase the signal/noise ratio for THz imaging and spectroscopy, but in combination with the recently developed sources of powerful THz pulses, will allow the observation of nonlinear THz effects and a variety of nonlinear spectroscopies (such as two-dimensional spectroscopy), which are highly informative. This should find a wide spectrum of applications in science, engineering, biomedical research and environmental monitoring.

We also develop a theory of the spoof plasmons propagating at the interface between a dielectric and a real conductor. The deviation from a perfect conductor is introduced through a finite skin depth. The possibilities of guiding and focusing of spoof plasmons are considered. Geometrical parameters of the structure are found which provide a good guiding of such modes. Moreover, the limit on the concentration by means of planar spoof plasmons in case of non-ideal metal is established. These properties of spoof plasmons are of great interest for THz technology.

INDEX WORDS: Nanoplasmonics, Surface plasmon polaritons, Adiabatic concentration, Full coherent control on nanoscale, Nanowedge, Terahertz, Coaxial waveguide, Spoof plasmons, Nanoscale, Nanofocus, Terahertz (THz) energy nanoconcentration

OPTICAL AND TERAHERTZ ENERGY CONCENTRATION ON THE NANOSCALE IN PLASMONICS

by

ANASTASIA RUSINA

A Dissertation Submitted in Partial Fulfillment of the Requirements for the Degree of

Doctor of Philosophy

in the College of Arts and Sciences

Georgia State University

2009

OPTICAL AND TERAHERTZ ENERGY CONCENTRATION ON THE NANOSCALE IN PLASMONICS

by

ANASTASIA RUSINA

Committee Chair: Dr. Mark I. Stockman

Committee: Dr. Vadym Apalkov

Dr. Nikolaus Dietz

Dr. Steven Manson

Dr. Unil Perera

Dr. Paul Wiita

Electronic Version Approved:

Office of Graduate Studies

College of Arts and Sciences

Georgia State University

December 2009

Acknowledgements

I would like to gratefully thank my advisor Professor Mark I. Stockman for his guidance, understanding and patience, and most importantly his friendship, during my graduate studies.

I would also like to express my gratitude to the members of my committee and Dr. Richard Miller.

I owe my deepest appreciation to my parents, Tatiana and Nikolai, and Maxim Durach for their support and encouragement.

Table of Contents

List of Figures

List of Abbreviations

LHM	left-handed material
SP	surface plasmon
SPP	surface plasmon polaritons
SERS	surface enhanced Raman scattering
SNOM	scanning near-field microscopy
SPASER	surface plasmon amplification by stimulated emission of radiation
IMI	insulator-metal-insulator
MIM	metal-insulator-metal
WKB	Wentzel-Kramers-Brillouin
THz	terahertz

Chapter 1. Introduction

1.1 Problem of Nanoconcentration

A goal of modern physics is to achieve faster speeds and smaller sizes. Pushing optics to the nanometer scale opens up new perspectives, phenomena and properties. Therefore, the ability to concentrate energy becomes one of the important tasks of physics. Historically, such a trend was motivated by the benefits of miniaturization and integration of electronic circuits for computer engineering. However, the development of nanooptics faces a fundamental barrier on the way to nanoconcentration of light. The Fourier transform relation between the three-dimensional space and the space of wave-vectors imposes the relationship between these two domains, which is also called the uncertainty principle in optics [1].

One of the consequences of the uncertainty principle is the diffraction limit [2], which poses restrictions on the size of localization of radiation. Namely, light rays will not intercept in one infinitely small point, but instead create a spot with width $\Delta = \lambda / \theta$, where θ is the opening angle of the beam and λ is the wavelength of light. This equation determines the resolving power of a microscope. From this relationship it follows that resolution is determined by the wavelength of the light, which is on a microscale for the visible part of the spectrum.

Another way to concentrate light one could think of would be to squeeze electromagnetic energy to the required size in an optical cavity with reflecting mirrors. When the cavity size is

decreased below $\lambda/2$, the possibility of exciting electromagnetic oscillations disappears. The physical reason is the lack of space to exchange energy between the electric and magnetic fields, which follows from Maxwell's equations.

From the examples mentioned above, it is clear that the concentration of light beyond the diffraction limit is one of the challenges of nanooptics. One of the proposed solutions is to employ the so-called negative refraction materials or left-handed materials (LHM), which promise subwavelength superfocusing [3]. Originally proposed by Veselago in 1968 [4], these materials have recently stimulated a new wave of interest [5-8]. Snell's law is reversed at the interface of a left-handed medium with a normal material. Therefore, light entering a LHM undergoes refraction opposite to that usually observed. In this case Snell's law is still valid, but index of refraction is negative. In a LHM the phase and group velocities have different signs $v_{ph} \cdot v_g < 0$, i.e. the phase of the plane wave and the energy flow propagate in opposite directions. The diffraction limit is due to the fact that information from the source is lost in the far field zone since the evanescent modes that exponentially decay do not reach the observer. A left-handed lens can restore the information contained in the evanescent waves by amplifying them [3]. This allows resolving objects only few nanometers across [9-11]. The resolution of the superlens is not limited by diffraction, but rather determined by how many evanescent waves can be restored. This in turn is restricted by the material loss and nonlocality (spatial dispersion) in the superlens material [12]. Such losses are substantial in the near-infrared and visible parts of the spectrum [13]. It has been recently shown [14], that any attempt to completely compensate for the optical

losses leads to disappearance of negative refraction. This follows from the fundamental principle of causality which restricts the applicability of LHM.

The purpose of this work is to develop alternative ways of energy concentration on the nanoscale. Subwavelength field localization can be achieved by adiabatic focusing of propagating surface plasmon polaritons (SPPs) that can convert them into surface plasmons (SPs). Localization of SPs is not limited by the diffraction limit, because a SP is a purely electric oscillation of energy.

1.2 Brief History of Plasmons

As a consequence of the Coulomb interaction, an interacting electron gas supports collective oscillations of electron density - the plasma oscillations. A quantum of the plasma oscillations is called a plasmon.

Long before scientists discovered surface plasmons, they were employed by artists to generate vibrant colors in the staining of church windows and in glass artifacts. The first scientific studies in which surface plasmons were observed were initiated in the beginning of the twentieth century. In 1902 R. Wood noticed anomalous characteristics in the optical reflection measurements of a metallic grating [15]. Using the Drude theory of metals and electromagnetic properties of small spheres derived by Rayleigh, J. C. Maxwell Garnett two years later described the bright colors of the metal doped glasses [16]. Gustav Mie in 1908 further developed this research by introducing a full electrodynamic theory of light scattering by spherical particles [17].

In 1951 Bohm and Pines developed a theory of a solid state interacting electron gas which resembled a classical plasma [18]. By analogy to earlier work on plasma oscillations in gas discharges [19, 20], Pines called these collective oscillations “plasmons” [21]. During the same year, 1956, U. Fano introduced the term “polariton” for coupled oscillation of bound electrons and light inside transparent media [22]. Finally in 1968, Ritchie and coworkers explained Wood’s anomaly in terms of surface plasmon resonances excited on the grating [23]. Experimental studies of surface plasmons were greatly promoted by the excitation methods of attenuated total internal reflection developed by Otto [24] and Kretschmann and Raether [25]. From this point, the properties of plasmons have been extensively investigated. Now plasmonics is a well-developed distinct branch of optics with multiple exiting applications. Some of the achievements of plasmonics include surface enhanced Raman scattering (SERS) [26, 27], which allows single-molecule sensing [28, 29]; scanning near-field optical microscopy (SNOM), which gives super-resolution [30, 31]; SPASER, which stands for surface plasmon amplification by stimulated emission of radiation, and many others [32]. The SPASER is the nanoplasmonic counterpart of the laser, which was originally proposed in Ref. [33] and has been recently realized experimentally [34].

1.3 Surface Plasmon Polaritons

1.3.1 Surface Plasmon Polaritons on a Metal-Dielectric Interface

Here I would like to present a brief description of surface electromagnetic waves that propagate on the metal-dielectric interface: Surface Plasmon Polaritons (SPPs). The fields of SPPs exponentially decay from the boundary. To determine the condition for the existence for such modes, consider an interface between two semi-infinite non-magnetic media with dielectric functions ε_1 and ε_2 separated by a planar interface at $z = 0$. The full set of Maxwell's equations in the absence of external sources can be expressed as follows [35, 36]:

$$\nabla \times \mathbf{H}_i = \frac{1}{c}\frac{\partial \mathbf{D}_i}{\partial t}, \tag{1.1}$$

$$\nabla \times \mathbf{E}_i = -\frac{1}{c}\frac{\partial \mathbf{B}_i}{\partial t} \tag{1.2}$$

$$\nabla \cdot \mathbf{D}_i = 0, \tag{1.3}$$

$$\nabla \cdot \mathbf{B}_i = 0, \tag{1.4}$$

where $i = 1$ for $z < 0$ and $i = 2$ for $z > 0$.

The curl equations (1.1) and (1.2) should be supplemented by material equations that describe relations between $\mathbf{D}$ and $\mathbf{E}$, as well as between $\mathbf{B}$ and $\mathbf{H}$:

$$\mathbf{D}_i = \varepsilon_i \mathbf{E}_i, \tag{1.5}$$

$$\mathbf{B}_i = \mu_i \mathbf{H}_i. \tag{1.6}$$

For non-magnetic materials, the magnetic permeability is $\mu = 1$.

Solutions to the system (1.1)-(1.6) are of two kinds: s-polarized (TE) and p-polarized (TM) depending on which of the fields **E** or **H** is transverse to the plane of incidence. In the case of non-magnetic media s-polarized surface oscillations do not exist; instead one needs to seek the conditions under which a traveling wave with the magnetic field **H** parallel to the interface (p-polarized wave) may propagate along the surface $z = 0$, with the fields tailing off into the positive $z > 0$ and negative $z < 0$ directions. Choosing the y axis along the propagating directions, one can write

$$H_{xi} = H_{xi}^{0} e^{-\kappa_i |z|} e^{i(k_i y - \omega t)}, \tag{1.7}$$

$$E_{y,z_i} = E_{y,z_i}^{0} e^{-\kappa_i |z|} e^{i(k_i y - \omega t)}, \tag{1.8}$$

where H_{xi}^{0}, $E_{y_i}^{0}$ and E_{zi}^{0} are constant amplitudes of the corresponding field components and k_i represents the magnitude of a wave vector that is parallel to the surface. Equations (1.1)-(1.8) lead to

$$i\kappa_1 H_{x1} = \frac{\omega}{c} \varepsilon_1 E_{y_1}, \tag{1.9}$$

$$i\kappa_2 H_{x2} = -\frac{\omega}{c} \varepsilon_2 E_{y_2}, \tag{1.10}$$

where

$$\kappa_i = \sqrt{k_i^2 - \varepsilon_i \frac{\omega^2}{c^2}}, \tag{1.11}$$

are decay constants. The boundary conditions imply that the components of electric and magnetic fields parallel to the surface must be continuous. Using equations (1.9) and (1.10), one can write the following system of equations

$$\frac{\kappa_1}{\varepsilon_1} H_{x1} + \frac{\kappa_2}{\varepsilon_2} H_{x2} = 0 , \tag{1.12}$$

$$H_{x1} - H_{x2} = 0 , \tag{1.13}$$

which have a solution, if

$$\frac{\varepsilon_1}{\kappa_1} + \frac{\varepsilon_2}{\kappa_2} = 0 . \tag{1.14}$$

Solving together Eqs. (1.11) and (1.14) yields

$$k = k_0 \sqrt{\frac{\varepsilon_1 \varepsilon_2}{\varepsilon_1 + \varepsilon_2}} , \tag{1.15}$$

$$\kappa_1 = k_0 \sqrt{-\frac{\varepsilon_1^2}{\varepsilon_1 + \varepsilon_2}} , \tag{1.16}$$

$$\kappa_2 = k_0 \sqrt{-\frac{\varepsilon_2^2}{\varepsilon_1 + \varepsilon_2}} , \tag{1.17}$$

where $k_0 = \omega / c$ is the vacuum wave vector. In order for the SPP mode to be well-localized, k, κ_1 and κ_2 should be almost real. If we assume that ε_1 and ε_2 are real, it follows from relations (1.15)-(1.17) that

$$\varepsilon_1 + \varepsilon_2 < 0 , \tag{1.18}$$

$$\varepsilon_1 \cdot \varepsilon_2 < 0 , \tag{1.19}$$

which means that one of the dielectric functions must be negative with an absolute value exceeding that of the other, i.e $\varepsilon_1 < 0$ and $|\varepsilon_1| > \varepsilon_2$. Metals have a negative real part of their dielectric function in a broad frequency range. Using experimental data from Ref. [13], real and imaginary parts of dielectric permittivity for silver and gold are plotted in Figure 1.1.

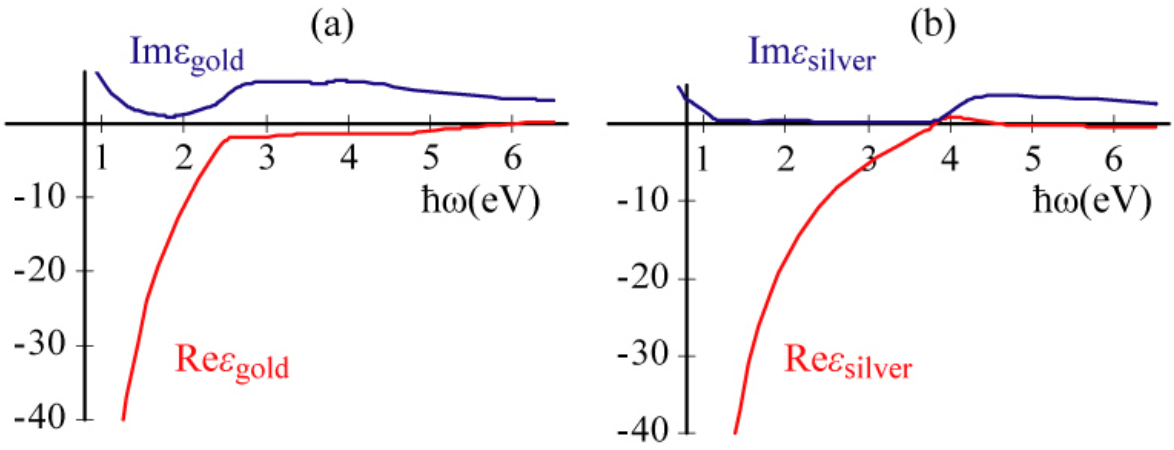

Figure 1.1. (color) Dielectric properties of metals. (a) Real (red) and imaginary (blue) part of dielectric function as the function of frequency $\hbar\omega$ for gold; (b) the same as in panel (a) but for silver.

Dielectrics and semiconductors also have negative dielectric function in the reststrahlen band between the frequencies of the transverse and longitudinal optical phonons [37].

According to the Drude model, the dielectric function of a free electron gas is [37]

$$\varepsilon(\omega) = \varepsilon_\infty - \frac{\omega_p^2}{\omega(\omega + i\Gamma)}, \tag{1.20}$$

where $\omega_p = \sqrt{4\pi n e^2/m}$ is the plasma frequency of the free electron gas, Γ is the collision frequency and ε_∞ is the background dielectric function. The Drude dielectric function, Eq. (1.20), adequately describes the optical response of metals for the frequencies lower than the frequency of the interband transition.

The dielectric function of real metals has also imaginary part (shown by the blue curve in Figure 1.1), which describes losses. Therefore, the condition of existence of a well-defined SPP should be written in the following way

$$\begin{gathered} \operatorname{Re}\varepsilon_1 + \operatorname{Re}\varepsilon_2 < 0\,, \quad \operatorname{Re}\varepsilon_1 \cdot \operatorname{Re}\varepsilon_2 < 0 \\ \operatorname{Im}\varepsilon_1 << \left|\operatorname{Re}\varepsilon_1\right|, \quad \operatorname{Im}\varepsilon_2 << \left|\operatorname{Re}\varepsilon_2\right|. \end{gathered} \tag{1.21}$$

According to Figure 1.1, silver has smaller imaginary part of dielectric function than gold; hence, it is more suitable for SPP propagation and other applications.

The dispersion relation Eq. (1.15) in case of silver/air interface is depicted in Figure 1.2(a). Since for real metal the permittivity is complex number, the wave vector is also complex. The presence of damping causes a backbending in the real part of wave vector (red curve in Figure 1.2(a)), i.e., $\mathrm{Re}\,k$ decreases with increase of frequency. When the SPP propagation constant k is close to k_0, SPP waves extend over many wavelengths into the dielectric. Such surface electromagnetic waves (SEW) are known as Sommerfeld-Zenneck waves [38, 39].

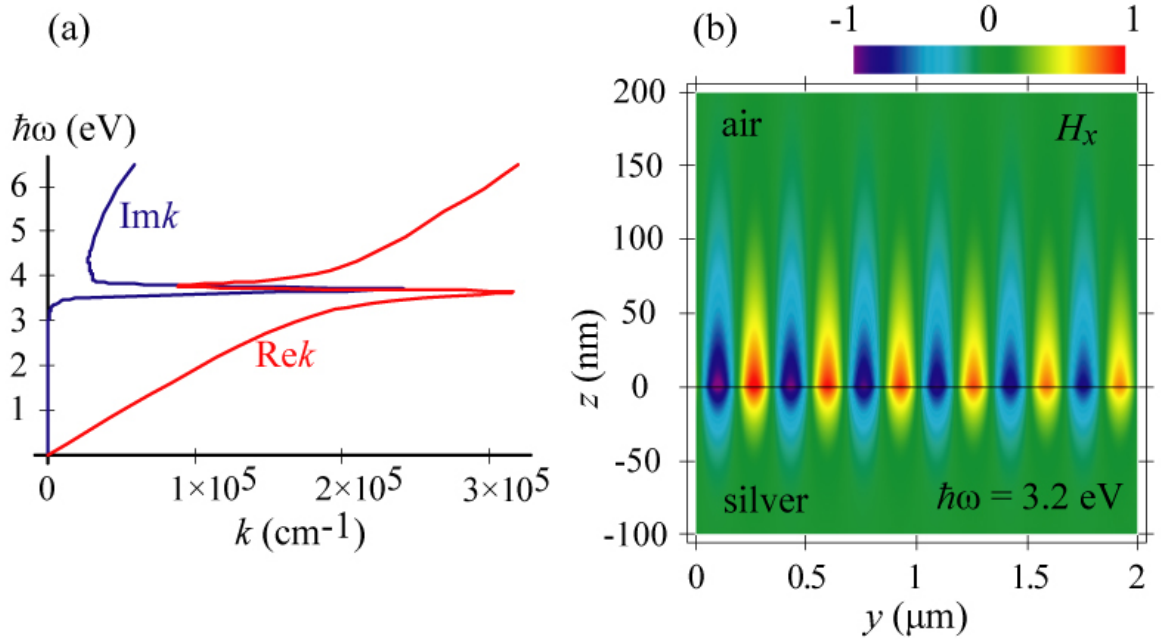

Figure 1.2. (color) (a) Dispersion relation of SPPs at silver/air interface. Real and imaginary parts of wave number are shown by the red and blue curves, respectively. (b) Distribution of magnetic field H_x shown in yz plane at the silver/air interface. The magnitude is coded by the color as shown by the bar.

The real part of the propagation constant determines the SPP wavelength, $\lambda = 2\pi / \mathrm{Re}\, k$, while the imaginary part of the wave number represents the characteristic propagation length, $l_p = 1/\mathrm{Im}\, k$, of SPPs.

Figure 1.2(b) shows the distribution of the transverse magnetic field H_x for the silver/air interface. The most distinctive feature of the field are the different penetrations into the media. The exponents given by equations (1.16) and (1.17) define the extension of the SPP local field into the air, $l_d = 1/\mathrm{Re}\,\kappa_d$, and into the metal, $l_s = 1/\mathrm{Re}\,\kappa_m$; the latter is also called the skin depth. As one can see from Figure 1.2(b), the field penetrates into dielectric more than into the metal due to the fact that the skin depth l_s is much smaller than the penetration length l_d in the visible and near-infrared frequency region.

1.3.2 Surface Plasmon Polaritons in Symmetric Layered Structures

Here let us consider SPP propagation in a symmetric three-layer system containing at least one metal layer. Each interface can support propagating SPPs. When the separation between two surfaces is comparable with the corresponding decay length, these SPPs start to couple with each other, creating new hybridized modes. Due to symmetry in this system, there can be odd and even modes. To derive dispersion relations for these modes, let us consider the system shown in Figure 1.3. If the system is symmetric the regions I and III are the same.

We seek a SPP as a solution of equations (1.1)-(1.6) that is bound to the layered system, has evanescent behavior in the regions I and III in Figure 1.3 and it a transverse magnetic (TM) mode.

Figure 1.3. Schematic picture of the three layer system.

The magnetic field for the odd (antisymmetric) mode can be written in the following form

$$H_x = A\, e^{i(ky-\omega t)} \begin{cases} e^{-\kappa_1 (z-a/2)}, & z > a/2 \\ \dfrac{\sinh(\kappa_2 z)}{\sinh(\kappa_2 a/2)}, & |z| < a/2\,, \\ -e^{\kappa_1 (z+a/2)}, & z < -a/2 \end{cases} \tag{1.22}$$

where κ_1 and κ_2 are given by the Eq. (1.11) and k is the component of the wave vector along the propagation direction. Here the magnetic field is already matched at the surfaces. Using the Maxwell's equations (1.1)-(1.4) together with material equations (1.5) and (1.6), one can find the components of the electric fields E_y and E_z as

$$E_y = -\frac{\partial_z H_x}{ik_0\varepsilon} = -\frac{A\, e^{i(ky-\omega t)}}{ik_0} \begin{cases} -(\kappa_1/\varepsilon_1) e^{-\kappa_1 (z-a/2)}, & z > a/2 \\ (\kappa_2/\varepsilon_2) \dfrac{\cosh(\kappa_2 z)}{\sinh(\kappa_2 a/2)}, & |z| < a/2\,, \\ -(\kappa_1/\varepsilon_1) e^{\kappa_1 (z+a/2)}, & z < -a/2 \end{cases} \tag{1.23}$$

$$E_z = \frac{\partial_y H_x}{ik_0\varepsilon} = \frac{Ake^{i(ky-\omega t)}}{k_0} \begin{cases} (1/\varepsilon_1) e^{-\kappa_1 (z-a/2)}, & z > a/2 \\ (1/\varepsilon_2) \dfrac{\sinh(\kappa_2 z)}{\sinh(\kappa_2 a/2)}, & |z| < a/2\,. \\ -(1/\varepsilon_1) e^{\kappa_1 (z+a/2)}, & z < -a/2 \end{cases} \tag{1.24}$$

The continuity of E_y at the boundaries leads to the dispersion relation for the odd mode

$$\tanh(\kappa_2 a/2) = -\frac{\varepsilon_1 \kappa_2}{\varepsilon_2 \kappa_1}. \tag{1.25}$$

The magnetic field of the even (symmetric) mode should be taken as

$$H_x = A\, e^{i(ky-\omega t)} \begin{cases} e^{-\kappa_1 (z-a/2)}, & z > a/2 \\ \dfrac{\cosh(\kappa_2 z)}{\cosh(\kappa_2 a/2)}, & |z| < a/2 \\ -e^{\kappa_1 (z+a/2)}, & z < -a/2 \end{cases}. \tag{1.26}$$

From this, the components of electric field are

$$E_y = -\frac{A\, e^{i(ky-\omega t)}}{ik_0} \begin{cases} -(\kappa_1/\varepsilon_1) e^{-\kappa_1 (z-a/2)}, & z > a/2 \\ (\kappa_2/\varepsilon_2) \dfrac{\sinh(\kappa_2 z)}{\cosh(\kappa_2 a/2)}, & |z| < a/2 \\ -(\kappa_1/\varepsilon_1) e^{\kappa_1 (z+a/2)}, & z < -a/2 \end{cases}, \tag{1.27}$$

$$E_z = \frac{Ake^{i(ky-\omega t)}}{k_0} \begin{cases} (1/\varepsilon_1) e^{-\kappa_1 (z-a/2)}, & z > a/2 \\ (1/\varepsilon_2) \dfrac{\cosh(\kappa_2 z)}{\cosh(\kappa_2 a/2)}, & |z| < a/2 \\ -(1/\varepsilon_1) e^{\kappa_1 (z+a/2)}, & z < -a/2 \end{cases}. \tag{1.28}$$

Similarly, the dispersion relation for the even mode is

$$\tanh(\kappa_2 a/2) = -\frac{\varepsilon_2 \kappa_1}{\varepsilon_1 \kappa_2}. \tag{1.29}$$

If the metal layer is embedded into a dielectric matrix (IMI structure), the dielectric functions are $\varepsilon_1 = \varepsilon_d$ and $\varepsilon_2 = \varepsilon_m$ and the dispersion relation for the odd mode (1.25) becomes

$$\tanh(\kappa_m a/2) = -\frac{\varepsilon_d \kappa_m}{\varepsilon_m \kappa_d}, \tag{1.30}$$

while for the even mode Eq. (1.29) is now the following

$$\tanh(\kappa_m a/2) = -\frac{\varepsilon_m \kappa_d}{\varepsilon_d \kappa_m}. \tag{1.31}$$

Figure 1.4 depicts the dispersion relations for the odd (Eq. (1.30)) and even (Eq. (1.31)) modes for two different thicknesses of the silver film. Solid curves in this figure are obtained for the width of metal film $a = 60\,nm$, which is more than two skin depths. In this case the interaction between SPPs localized at the metal-vacuum interface is relatively weak and difference between odd (red curve) and even (blue curve) SPP modes is not very large. On the other hand, when $a = 25\,\text{nm}$, which is approximately one skin depth, there should be strong mixing of two SPPs modes at the two surfaces of the metal layer. Indeed, there is a large contrast between even and odd modes, shown by the broken lines in Figure 1.4.

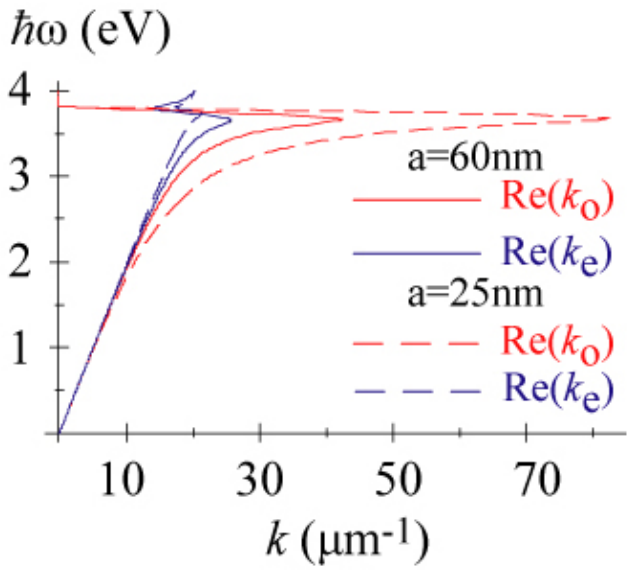

Figure 1.4. (color) Dispersion relations as functions of frequency $\hbar\omega$ on the real part of wave vector k. The computation is done for odd (red curves) and even (blue curves) modes of the nanometric silver layer in air. Solid lines correspond to the thickness of the silver film $a = 60\,\text{nm}$, while broken lines represent modes in layer of thickness $a = 25\,\text{nm}$.

The symmetry of the modes is usually determined by the transverse fields E_z. An E_z symmetric with respect to the film mid-plane transverse component corresponds to an

antisymmetric longitudinal component, E_y, and vice versa. Usually metals exhibit large magnitudes of the dielectric permittivities, i.e. $|\varepsilon_m| >> \varepsilon_d$. Therefore the normal component E_z is dominant in the dielectric while the tangential component E_y is dominant in the metal. As a result, SPP electric field is primarily transverse in the dielectric and longitudinal in metal. Since the SPP attenuation occurs due to ohmic losses in metal, it is the longitudinal electric field component E_y of the SPP in metal that determines the SPP damping. In Figure 1.5, the longitudinal component of electric field E_y is plotted for symmetric (a) and anti-symmetric (b) modes.

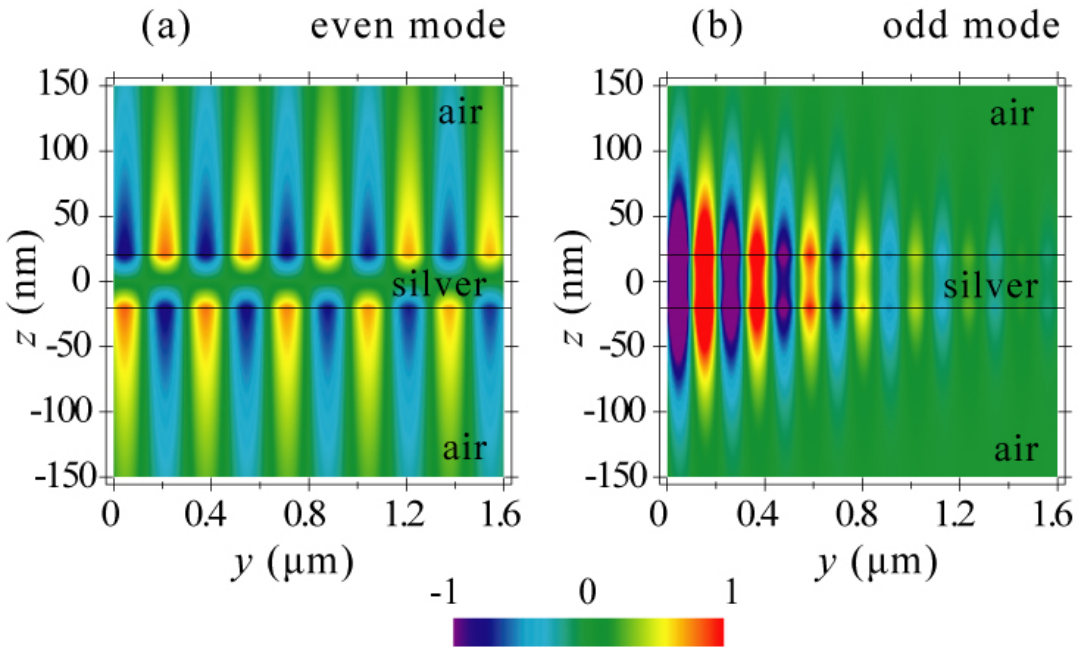

Figure 1.5. (color) Distribution in space of longitudinal electric field E_y in the yz plane of propagation. The frequency of the SPP is chosen to be $\hbar\omega = 3.4\,\text{eV}$. The thickness of the silver film is $a = 40\,\text{nm}$. (a) E_y of the even mode (b) E_y of the odd mode.

The symmetric SPP mode exhibits the odd symmetry of E_y, so that it is zero at the middle plane of the metal film. Consequently, the symmetric mode experiences smaller damping than

the antisymmetric mode with a symmetric E_y configuration. This behavior is confirmed in Figure 1.5.

Other properties of even and odd modes can be obtained by investigating the dispersion relations for the thin films ($a \to 0$), i.e., when one can use the approximation $\tanh x \approx x$. Eq. (1.31) for even mode in case of the very thin films after straightforward algebra becomes

$$k_{even} = k_0 \sqrt{\varepsilon_d + \left(\frac{k_0 a \varepsilon_d}{2}\right)^2 \left(1 - \frac{\varepsilon_d}{\varepsilon_m}\right)^2} \,. \tag{1.32}$$

When $a \to 0$, the wave number of the even mode approaches the light line ($k = k_0 \sqrt{\varepsilon_d}$) in the dielectric. For this mode, with a decrease of the thickness of the layer, the losses would decrease to zero, while the propagation length increases to infinity.

The more interesting properties for the purpose of concentration exhibit the odd mode in metal films. When the thickness tends to zero, we can approximate k in Eq. (1.30) as

$$k_{odd} = k_0 \sqrt{\varepsilon_d + \left(\frac{2\varepsilon_d}{k_0 a \varepsilon_m}\right)^2} \,. \tag{1.33}$$

Contrary to the behavior of the even modes in case of thin films, the wavelength and propagation length of the odd mode decrease with a decrease of the thickness of the film. This mode is more controllable and we will use it in the next Chapter to produce nanoconcentration of light.

Now let us turn to the description of the system consisting of the dielectric layer embedded in metal matrix (MIM structure). Thus, regions I and III in Figure 1.3 are metals and region II is a dielectric. The properties of the SPPs in this system are different from those of SPPs in metal film. The equations (1.25) and (1.29) change to

$$\tanh\left(\kappa_d a/2\right) = -\frac{\varepsilon_m \kappa_d}{\varepsilon_d \kappa_m} \tag{1.34}$$

for the odd mode and

$$\tanh\left(\kappa_d a/2\right) = -\frac{\varepsilon_d \kappa_m}{\varepsilon_m \kappa_d} \tag{1.35}$$

for the even mode.

In Figure 1.6, one can see the dispersion of these two modes. The odd mode is denoted by the red color with the solid line corresponding to the real part of wave vector and broken line to its imaginary part. The dispersion relation of the even mode is similarly shown in the blue color. Obviously, these two modes possess different qualities than for IMI case. Now even and odd modes have backbending, with the maximum values of $\mathrm{Re}\,k$ at around $\omega_{SP} = \omega_p/\sqrt{2}$, which is the frequency of a static plasmon at the metal/dielectric interface. It is interesting to compare the imaginary parts of k of these modes. For the even mode, $\mathrm{Re}\,k_e$ mostly dominates over $\mathrm{Im}\,k_e$; consequently, it is well-defined excitation. Contrary to this, $\left|\mathrm{Im}\,k_o\right| > \mathrm{Re}\,k_o$, i.e., the imaginary part of the wave number of the odd mode is larger than its real part in the entire considered spectral region, showing that this mode does not propagate in this system. Moreover, the odd mode is a negative refraction mode since $\mathrm{Re}\,k_o \cdot \mathrm{Im}\,k_o < 0$. Therefore, this mode is not very useful in a such system and later in Chapter 3 we will use the even mode for the purpose of nanoconcentration of terahertz radiation.

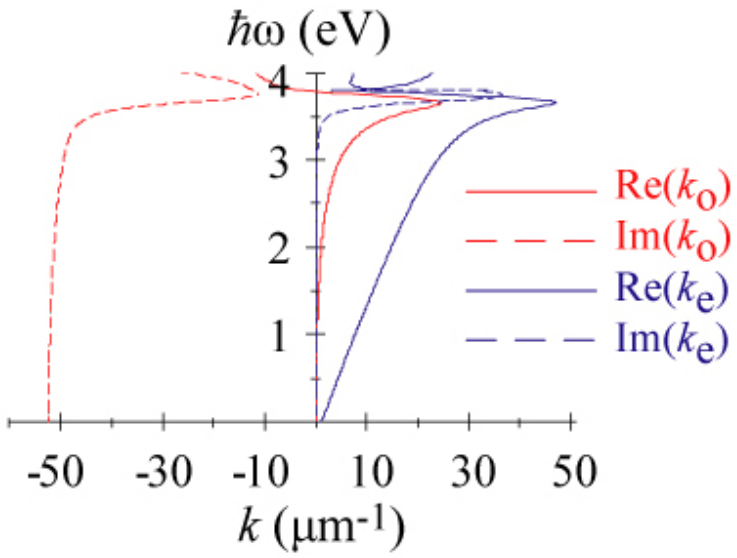

Figure 1.6. (color) Dispersion relation of the modes in a metal/dielectric/metal structure. Odd and even modes are shown by the red and blue colors, respectively. Solid curves represent real parts of the wave vectors and broken lines their imaginary parts. The thickness of the dielectric film (air) is $a = 60\,\text{nm}$ and the metal is silver with a dielectric function from Ref. [13].

1.4 Adiabatic Concentration of Electromagnetic Fields

The original work introduced in this paper is devoted to the concentration of the optical and terahertz energy to the nanoscale. One can think of two ways to concentrate radiation: adiabaticaly or non-adiabaticaly (abruptly). Evidently, the adiabatic way of concentration has several advantages. If energy is concentrated adiabatically, it adjusts to the changing system without scattering and reflection. This means that adiabatic concentration is highly efficient. But this advantage makes adiabatic concentration more demanding. At each intermediate size there should be an optical mode in which energy can be stored. Therefore, light and modes in waveguides with cut-offs are not suitable for the adiabatic concentration process. The requirement of having the proper mode at each size makes SPPs perfect for this purpose. The

possibility of the adiabatic concentration of the propagating SPP was first introduced in Ref. [40], where SPP are adiabatically transformed into the localized SP with reduction of the size of the system.

The theory of the adiabatic concentration is described within the frame of geometrical optics, and is often called the Wentzel-Kramers-Brillouin (WKB), or Eikonal, approximation [41]. WKB is applicable if the variation of the structure parameters is small on one wavelength of the field. In this case, we may assume that the field, φ, which can be any component of $\mathbf{E}$ or $\mathbf{H}$, will adjust gradually to these parameters and the field will also change slowly in space, and hence may locally be represented by an almost plane wave

$$\varphi(\mathbf{r}) = A(\mathbf{r})e^{i\Phi(\mathbf{r})}, \tag{1.36}$$

where the amplitude $A(\mathbf{r})$ and phase (eikonal) $\Phi(\mathbf{r})$ are slowly varying functions of $\mathbf{r}$, i.e., they change insignificantly within the regions on the scale of λ. The eikonal $\Phi(\mathbf{r})$ satisfies the following equation

$$(\nabla\Phi(\mathbf{r}))^2 = k^2, \tag{1.37}$$

where k is the wave vector. There are two ways to find the amplitude $A(\mathbf{r})$. One can substitute Eq. (1.36) into Maxwell equations (1.1)-(1.4) and expand the result over the small parameter related the adiabaticity of the problem. The second method is to use the conservation of energy flux of the solution (1.36).

This nanoconcentration, as described by the WKB approximation, is possible in cylinders or in thin metal or dielectric slabs, when the thickness and radius of these geometries are

adiabatically decreased along the direction of propagation. The SPP modes they support become more strongly confined and concentrated to very small dimensions. This effect was demonstrated both theoretically [40, 42, 43] and experimentally [44, 45].

Chapter 2. Coherently Controlled Nanoconcentration of Optical Energy

2.1 Introduction

Two novel areas of optics have recently attracted a great deal of attention: nanooptics and ultrafast optics. One of the most important directions in ultrafast optics is quantum control, in which the coherent superpositions of quantum states are created by excitation radiation to control the quantum dynamics and outcomes [46-49]. Of special interest are coherently controlled ultrafast phenomena on the nanoscale where the phase of the excitation waveform provides a functional degree of freedom to control the nanoscale distribution of energy [50-56]. Spatio-temporal pulse shaping permits one to generate dynamically predefined waveforms modulated both in frequency and in space to focus ultrafast pulses in the required microscopic spatial and femtosecond temporal domains [57, 58].

In the paper [43], we have proposed and theoretically developed a method of full coherent control on the nanoscale where a spatio-temporal modulated pulse is launched in a graded nanostructured system, specifically in a wedge. Its propagation and adiabatic concentration provide a possibility to focus optical energy in nanoscale spatial and femtosecond temporal regions. Our method unifies three approaches that individually have been developed and experimentally tested. The coupling of the external radiation to the surface plasmon polaritons

(SPPs) propagating along the wedge occurs through an array of nanoobjects (nanoparticles or nanoholes) that is situated at the thick edge of the wedge. The phases of the SPPs emitted (scattered) by individual nanoobjects are determined by a spatiotemporal modulator. The nanofocusing of the SPPs occurs due to their propagation toward the nanofocus and the concurrent adiabatic concentration.

The coupling of the external radiation to SPPs and their nanofocusing has been observed in [59, 60]. The second component of our approach, the spatiotemporal coherent control of such nanofocusing, has been developed in [57, 58]. The third component, the adiabatic concentration of SPPs, also has been recently observed [45, 61]. The idea of adiabatic concentration is based on adiabatic following by a propagating SPP wave of a graded plasmonic waveguide, where the phase and group velocities decrease while the propagating SPP wave is adiabatically transformed into a standing surface plasmon (SP) mode [40, 42, 62]. The theory on which this method is based is described in more detail in Section 1.4. A new quality that is present in our approach is the possibility to arbitrarily move the nanofocus along the nanoedge of the wedge. Moreover, it is possible to superimpose any number of such nanofoci simultaneously and, consequently, create any distribution of the nanolocalized fields at the thin edge of the wedge.

2.2 Concept

Consider first the adiabatic concentration of a plane SPP wave propagating along a nanowedge of silver [13], as shown in Figure 2.1(a); the theory is based on the Wentzel-Kramers-Brillouin (WKB) or quasiclassical approximation, also called the eikonal

approximation [41], briefly described in Section 1.4. The propagation velocity of the SPP along such a nanowedge is asymptotically proportional to its thickness. Thus when a SPP approaches the sharp edge, it slows down and asymptotically stops. In a real system with a sharp edge of finite thickness (below we consider a 4 nm limit, well within the achievable range), there is very substantial slowing down, nanofocusing and increase in field amplitude.

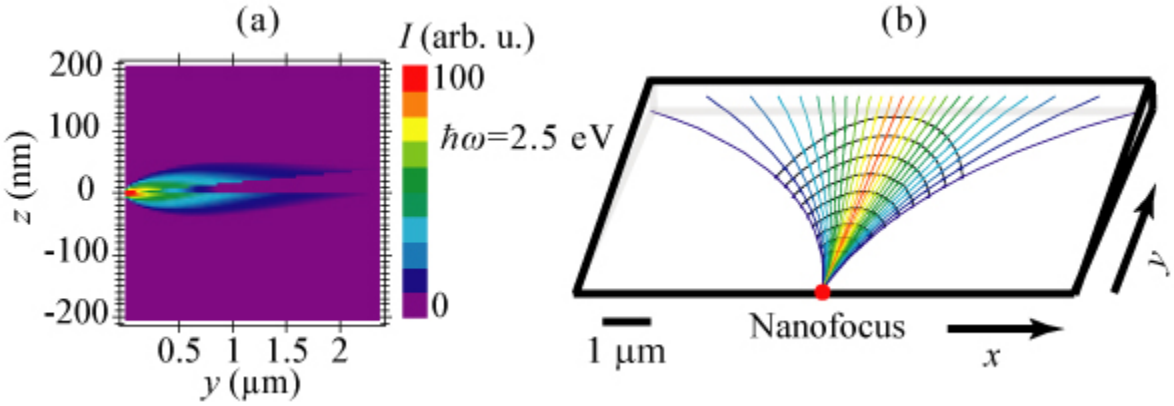

Figure 2.1. (color) (a) Illustration of adiabatic concentration of energy on the wedge. The distribution of local field intensity I in the normal plane of propagation of SPPs (the yz plane). The intensity in relative units is color coded with the color scale bar shown to the right. This intensity distribution is obtained after Eq. (2.11). (b) Trajectories of SPP rays propagating from the thick to sharp edge of the wedge. The initial coordinate is coded with color. The black curves indicate lines of equal phase (SPP wavefronts).

To illustrate the idea of this full coherent control, now consider a wedge that contains a line of nanosize scatterers (say, nanoparticles or nanoholes) located at the thick edge and parallel to it, i.e., in the x direction in Figure 2.1(b). Consider first monochromatic light irradiating these nanoparticles or nanoholes that scatter and couple it into SPP wavelets. Every such scatterer emits SPPs in all directions; there is, of course, no favored directionality of the scattering. However, we assume that the excitation radiation and, correspondingly, the scattered wavelets of the SPP are coherent, and their phases smoothly vary in space along the thick edge, i.e., in the x

direction. The SPP wavelets emitted by different scatterers will interfere, which in accord with the Huygens-Fresnel principle leads to formation of a smooth wavefront of the SPP wave at some distance from the scatterers in the far SPP field.

Such wave fronts are shown in Figure 2.1(b) with concave black curves. The energy of the SPP is transferred along the rays, which are lines normal to the wavefronts, shown by the colored lines. By the appropriate spatial phase modulation of the excitation radiation along the line of scatterers over distances of many SPP wavelengths, these wavefronts can be formed in such a way that the rays intersect at a given point, forming a nanofocus at the thin (sharp) edge of the wedge, as shown schematically in Figure 2.1(b). Diffraction of the SPP waves will lead to a finite size of this focal spot that we will estimate later in this Chapter.

By changing the spatial phase profile of the excitation radiation, this focal spot can be arbitrarily moved along the thin edge. This focusing and adiabatic concentration, as the SPPs slow down approaching the sharp edge, will lead to the enhancement of the intensity of the optical fields in the focal region. This dynamically controlled concentration of energy is a plasmonic counterpart of a large phased antenna array (also known as an aperture synthesis antenna or beamformer), widely used in radar technology and radio astronomy [63]. Now we can consider excitation by spatiotemporally shaped ultrashort pulses [57, 58]. The field produced by them is a coherent superposition of waves with different frequencies whose amplitudes and phases can arbitrarily vary in space and with frequency. This modulation can be chosen so that all the frequency components converge at the same focal spot at the same time, forming an ultrashort pulse of the nanolocalized optical fields.

2.3 Basic Equations

Turning to the theory, consider a nanofilm of metal in the xy plane whose thickness a in the z direction is adiabatically changing with the coordinate-vector $\boldsymbol{\rho}=(x,y)$ in the plane of the nanofilm. Let $\varepsilon_m=\varepsilon_m(\omega)$ be the dielectric permittivity of this metal nanofilm, and ε_d be the permittivity of the embedding dielectric. Because of the symmetry of the system, there are odd and even (in the normal electric field) SPPs. It is the odd SPP that is a slow-propagating, controllable mode, whose properties was discussed in Subsection 1.3.2. The fields for this mode are given by equations (1.22)-(1.24). The dispersion relation for this mode [see (1.30)] is

$$\tanh\left(\frac{1}{2}k_0 a(\boldsymbol{\rho})\sqrt{n(\boldsymbol{\rho})^2-\varepsilon_m}\right)=-\frac{\varepsilon_d\sqrt{n(\boldsymbol{\rho})^2-\varepsilon_m}}{\varepsilon_m\sqrt{n(\boldsymbol{\rho})^2-\varepsilon_d}}, \tag{2.1}$$

where $k_0=\omega/c$ is the radiation wave vector in vacuum and $n(\boldsymbol{\rho})$ is the effective index of refraction.

Let $\boldsymbol{\tau}$ be a unit tangential vector to the SPP trajectory (ray). It obeys an equation of ray optics [41]

$$n\left(\frac{d\boldsymbol{\tau}}{dl}\right)=\frac{\partial n}{\partial\boldsymbol{\rho}}-\boldsymbol{\tau}\left(\boldsymbol{\tau}\frac{\partial n}{\partial\boldsymbol{\rho}}\right), \tag{2.2}$$

where l is the length along the ray.

Now let us consider a nanofilm shaped as a nanowedge as in Figure 2.1(b). In such a case, $n=n(y)$, and these trajectory equations simplify to

$$n\left(\frac{d\tau_y}{dl}\right)=\tau_x^2\frac{\partial n}{\partial y},\qquad n\left(\frac{d\tau_x}{dl}\right)=-\tau_x\tau_y\left(\frac{\partial n}{\partial y}\right). \tag{2.3}$$

From these, it follows that $\frac{d(\tau_x n)}{dl} = \frac{dn}{dy}\left(\frac{dy}{dl}\right)\tau_x - \tau_x \tau_y \frac{dn}{dy} = 0$, i.e., $n_x \equiv \tau_x n = const$. The SPP wave vector, related to its momentum, is $\mathbf{k}(\boldsymbol{\rho}) = k_0 n(\boldsymbol{\rho})\boldsymbol{\tau}$; this is the conservation of k_x (the transverse momentum). This allows one to obtain a closed solution for the ray. The tangent equation for the ray is $dx/dy = \tau_x/\tau_y$, where $\tau_y = \sqrt{1 - n_x^2/n^2}$. From this, we get an explicit SPP ray equation as

$$x - x_0 = \int_{y_0}^{y} \left(\frac{n(y')^2}{n_x^2} - 1 \right)^{-1/2} dy' . \tag{2.4}$$

where $\boldsymbol{\rho}_0 = (x_0, y_0)$ is the focal point where rays with any n_x converge. To find the trajectories, we use the real part of the effective index (Eq.(2.1)), as WKB suggest.

When the local thickness of the wedge is subwavelength $(k_0 a << 1)$, the form of these trajectories can be found analytically. Under these conditions, the dispersion relation Eq.(2.1) has an asymptotic solution

$$n = \frac{n_{as}}{k_0 a} \qquad n_{as} = \ln \frac{\varepsilon_m - \varepsilon_d}{\varepsilon_m + \varepsilon_d} . \tag{2.5}$$

Substituting this into Eq. (2.4), we obtain an explicit SPP ray equation

$$\left(x - x_0 - \sqrt{\bar{n}_{as}^2 / n_x^2 - y_0^2} \right)^2 + y^2 = \bar{n}_{as}^2 / n_x^2 , \tag{2.6}$$

where $\bar{n}_{as} = n_{as}/(k_0 \tan\theta)$ and $\tan\theta$ is the slope of the wedge. Thus, each SPP ray is a segment of a circle whose center is at a point given by $x = x_0 + \sqrt{\bar{n}_{as}^2 / n_x^2 - y_0^2}$ and $y = 0$. This analytical result is in agreement with Figure 2.1(b). If the nanofocus is at the sharp edge, i.e., $y_0 = 0$, then these circles do not intersect but touch and are tangent to each other at the nanofocus point.

The eikonal, or phase, can be found as an integral along the ray $\Phi(\boldsymbol{\rho}) = k_0 \int_{\rho 0}^{\rho} \mathbf{n}(\boldsymbol{\rho}) d\boldsymbol{\rho}$, where $n(\boldsymbol{\rho})$ is the solution of Eq. (2.1).

Finally, the evolution of the field intensity along a SPP ray should be considered. For certainty, let SPPs propagate along the corresponding rays from the thick edge of the wedge toward the nanofocus as shown in Figure 2.1(b). In the process of such propagation, there will be concentration of the SPP energy in all three directions (3D nanofocusing). This phenomenon differs dramatically from what occurs in conventional photonic ray optics. To describe this 3D nanofocusing, it is convenient to introduce an orthogonal system of ray coordinates whose unit vectors are $\boldsymbol{\tau}$ (along the ray), $\boldsymbol{\eta} = \left(-\tau_y, \tau_x\right)$ (at the surface normal to the ray), and $\mathbf{e}_z$ (normal to the surface). The concentration along the ray (in the $\boldsymbol{\tau}$ direction) occurs because the group velocity $\upsilon_g = \left[\partial\left(k_0 n\right)/\partial\omega\right]^{-1}$ of the SPP asymptotically tends to zero (for the odd mode) for $k_0 a \to 0$ as $\upsilon_g = \upsilon_{0g} a$, where $\upsilon_{0g} = const$. This contributes a factor $A_{\|} = 1/\sqrt{\upsilon_g(a)}$ to the amplitude of an SPP wave.

The compression of a SPP wave in the $\mathbf{e}_z$ (vertical) direction is given by a factor of $A_z = \left(\int_{-\infty}^{\infty} W dz \right)^{-1/2}$, where the energy density of the mode W is equal to [41]

$$W = \frac{1}{4\pi} \left\{ \mathrm{Re} \frac{\partial\left(\omega\varepsilon(\omega)\right)}{\partial\omega} |\mathbf{E}|^2 + |\mathbf{H}|^2 \right\}. \tag{2.7}$$

Using the field equations (1.22)-(1.24), one can write energy density in the following way

$$W = \frac{1}{4\pi}\begin{cases} \left(\dfrac{|k|^2 + |\kappa_d|^2}{k_0^2 \varepsilon_d} + 1\right) e^{-2\,\mathrm{Re}\,\kappa_d (z - a/2)}, & z > a/2 \\ \dfrac{\partial(\omega\,\mathrm{Re}\,\varepsilon_m)}{\partial\omega} \dfrac{|k\sinh(\kappa_m z)|^2 + |\kappa_m \cosh(\kappa_m z)|^2}{|\varepsilon_m|^2 k_0^2 \left|\sinh\left(\kappa_m \dfrac{a}{2}\right)\right|^2} + \dfrac{|\sinh(\kappa_m z)|^2}{\left|\sinh\left(\kappa_m \dfrac{a}{2}\right)\right|^2}, & |z| < a/2 \\ \left(\dfrac{|k|^2 + |\kappa_d|^2}{k_0^2 \varepsilon_d} + 1\right) e^{2\,\mathrm{Re}\,\kappa_d (z + a/2)}, & z < -a/2 \end{cases} \tag{2.8}$$

The next step is to use the relations

$$\begin{aligned} |\sinh(\kappa_m z)|^2 &= (\cosh(2\,\mathrm{Re}\,\kappa_m z) - \cos(2\,\mathrm{Im}\,\kappa_m z))/2 \\ |\cosh(\kappa_m z)|^2 &= (\cosh(2\,\mathrm{Re}\,\kappa_m z) + \cos(2\,\mathrm{Im}\,\kappa_m z))/2 \end{aligned} . \tag{2.9}$$

Noticing that the intervals from $z > a/2$ and $z < -a/2$ will contribute equally into the integrals, the factor of the compression along the z direction is

$$\begin{aligned} 4\pi A_z^{-2} &= 2\left(\frac{|k|^2 + |\kappa_d|^2}{k_0^2 \varepsilon_d} + 1\right) \int_{a/2}^{\infty} e^{-2\,\mathrm{Re}\,\kappa_d (z - a/2)} dz + \\ &+ \frac{2\partial(\omega\,\mathrm{Re}\,\varepsilon_m)/\partial\omega}{|\varepsilon_m|^2 k_0^2 |\sinh(\kappa_m a/2)|^2} \left[\frac{|k|^2 + |\kappa_m|^2}{2} \left(\int_0^{a/2} \cosh(2\,\mathrm{Re}\,\kappa_m z) dz \right) - \right. \\ &\left. - \frac{|k|^2 - |\kappa_m|^2}{2} \left(\int_0^{a/2} \cos(2\,\mathrm{Im}\,\kappa_m z) dz \right) \right] + \\ &+ \frac{1}{|\sinh(\kappa_m a/2)|^2} \int_0^{d/2} [\cosh(2\,\mathrm{Re}\,\kappa_m z) - \cos(2\,\mathrm{Im}\,\kappa_m z)] dz \end{aligned} . \tag{2.10}$$

Evaluation of these integrals leads to the final expression for the compression factor along the z direction:

$$4\pi A_z^{-2} = \frac{1}{\operatorname{Re}\kappa_d}\left(\frac{|k|^2+|\kappa_d|^2}{k_0^2\varepsilon_d}+1\right)e^{\operatorname{Re}\kappa_d a} + \frac{\partial(\omega\operatorname{Re}\varepsilon_m)/\partial\omega}{k_0^2|\varepsilon_m\sinh(\kappa_m a/2)|^2}\left[\frac{|k|^2+|\kappa_m|^2}{2\operatorname{Re}\kappa_m}\sinh(\operatorname{Re}\kappa_m a)-\frac{|k|^2-|\kappa_m|^2}{2\operatorname{Im}\kappa_m}\sin(\operatorname{Im}\kappa_m a)\right]+ \frac{1}{2|\sinh(\kappa_m a/2)|^2}\left[\frac{\sinh(\operatorname{Re}\kappa_m a)}{\operatorname{Re}\kappa_m}-\frac{\sin(\operatorname{Im}\kappa_m a)}{\operatorname{Im}\kappa_m}\right] \tag{2.11}$$

where $\kappa_m = k_0\sqrt{n-\varepsilon_m}$ and $\kappa_d = k_0\sqrt{n-\varepsilon_d}$. Note that the intensity distribution in Figure 2.1(a) is $I \propto \left(A_{\|}A_z\right)^{-2}$.

To obtain the compression factor $A_\perp$ for the $\boldsymbol{\eta}$ direction, we consider conservation of energy flux along the beam of rays corresponding to slightly different values of n_x. Variation of trajectory Eq. (2.4) over n_x gives

$$\delta x = \left(\frac{n(y)^2}{n_x^2}-1\right)^{-1/2}\delta y + \delta n_x\int_{y_0}^{y}\frac{n(y')^2}{n_x^3}\left(\frac{n(y')^2}{n_x^2}-1\right)^{-3/2}dy'. \tag{2.12}$$

In order to find the connection between δy and δx, one should use the equation $\delta y/\delta x = \eta_y/\eta_x$, where $\boldsymbol{\eta} = \left(-\sqrt{1-\left(n_x/n(y)\right)^2}, n_x/n(y)\right)$ is a unit vector along the wavefront. Therefore, variation of y is $\delta y = -\delta x\left(\left(n(y)/n_x\right)^2-1\right)^{-1/2}$. Substituting such variation of y in Eq. (2.12), we obtain the following relations for the variations of x and y

$$\delta x = \left(\frac{n(y)^2}{n_x^2}-1\right)\left(\frac{n_x}{n(y)}\right)^2\delta n_x\int_{y_0}^{y}\frac{1}{n(y')}\left(1-\frac{n_x^2}{n(y')^2}\right)^{-3/2}dy', \tag{2.13}$$

$$\delta y = -\left(\frac{n(y)^2}{n_x^2}-1\right)^{1/2}\left(\frac{n_x}{n(y)}\right)^2\delta n_x\int_{y_0}^{y}\frac{1}{n(y')}\left(1-\frac{n_x^2}{n(y')^2}\right)^{-3/2}dy'$$

The displacement of the trajectory along the wavefronts due to the variation of n_x can be written as

$$\delta s = \sqrt{\delta x^2 + \delta y^2} = \left(1 - \frac{n_x^2}{n(y)^2}\right)^{1/2} \delta n_x \int_{y_0}^{y} \frac{1}{n(y')} \left(1 - \frac{n_x^2}{n(y')^2}\right)^{-3/2} dy' . \tag{2.14}$$

Dividing the constant energy flux by the thickness of this beam δs in the $\boldsymbol{\eta}$ direction, we arrive at

$$A_\perp = \left\{ \left(1 - \frac{n_x^2}{n(y)^2}\right)^{1/2} \int_{y_0}^{y} \frac{1}{n(y')} \left(1 - \frac{n_x^2}{n(y')^2}\right)^{-3/2} dy' \right\}^{-1/2} . \tag{2.15}$$

The ray amplitude thus contains the total factor which describes the 3d adiabatic compression: $A = A_{\|} A_\perp A_z$, where $A_{\|} = \sqrt{d(k_0 n)/d\omega}$, A_z and $A_\perp$ are given by Eqs. (2.11) and (2.15), correspondingly.

2.4 Results and Discussions

Using the theory which is derived in Section 2.3, we consider a silver nanowedge illustrated in Figure 2.1(b) whose maximum thickness is $a_m = 30nm$, the minimum thickness is $a_f = 4nm$, and whose length (in the y direction) is $L = 5\mu m$. Trajectories calculated from Eq. (2.4) for $\hbar\omega = 2.5eV$ are shown by lines (color used only to guide eye); the nanofocus is indicated by a bold red dot. The different trajectories correspond to different values of n_x in the range $0 \le n_x \le n(L)$. In contrast to focusing by a conventional lens, the SPP rays are progressively bent toward the wedge slope direction.

Consider rays emitted from the nanofocus (Figure 2.1(b)). The real and imaginary parts of the phases $\Phi(\boldsymbol{\rho})$ of the SPPs at the thick edge of the wedge (for $y = L$) are shown in Figure 2.2(a) as functions of the coordinate x along the thick edge. The colors of the rays correspond to the visual perception of the ray frequencies. The gained phase dramatically increases toward

the blue spectral region, exhibiting a strong dispersion. The extinction for most of the frequencies except for the blue edge, displayed in Figure 2.2(b), is not high.

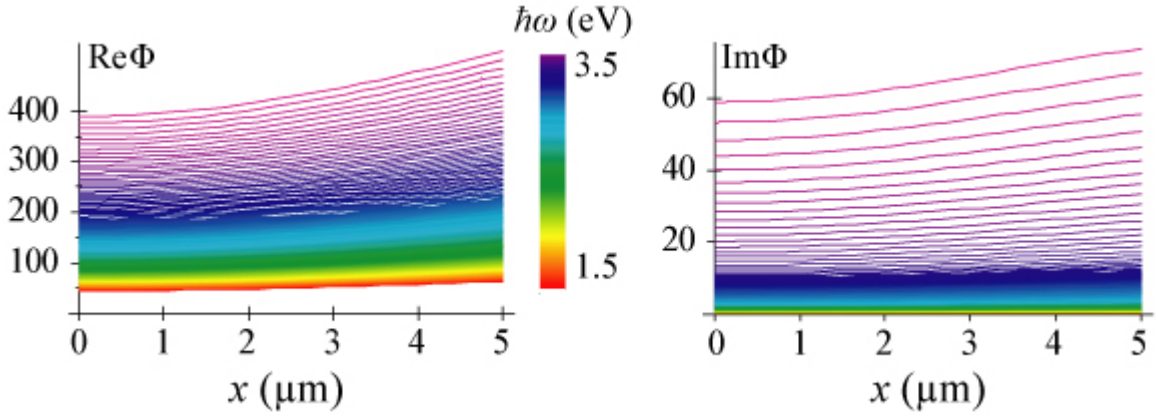

Figure 2.2. (color) (a) Phase (real part of eikonal Φ) acquired by a SPP ray propagating between a point with coordinate x on the thick edge and the nanofocus, displayed as a function of x. The rays differ by frequencies that are color coded by the vertical bar. (b) The same as (a) but for extinction of the ray, $\mathrm{Im}\,\Phi$.

Now consider the problem of coherent control. The goal is to excite a spatiotemporal waveform at the thick edge of the wedge in such a way that the propagating SPP rays converge at an arbitrary nanofocus at the sharp edge where an ultrashort pulse is formed. To solve this problem, we use the idea of back-propagation or time reversal [64-66].

We generate rays at the nanofocus as an ultrashort pulse containing just several oscillations of the optical field. By propagating these rays, we find amplitudes and phases of the fields at the thick edge at each frequency as given by the eikonal $\Phi(\boldsymbol{\rho})$. Then we complex conjugate the amplitudes of frequency components, which corresponds to the time reversal. We also multiply these amplitudes by $\exp(2\,\mathrm{Im}\,\Phi)$, which precompensates for the losses. This provides the required phase and amplitude modulation at the thick edge of the wedge.

We show an example of such calculations in Figure 2.3 for the silver nanowedge, with dielectric function taken from Ref. [13]. Panel (a) displays the trajectories of SPPs calculated according to Eq (2.4). The trajectories for different frequencies are displayed by colors corresponding to their visual perception. There is a very significant spectral dispersion: trajectories with higher frequencies are much more curved. The spatial-frequency modulation that we have found succeeds in bringing all these rays to the same nanofocus at the sharp edge.

The required waveforms at different x points of the thick edge of the wedge are depicted in Figure 2.3(b)-(d), where the corresponding longitudinal electric fields are shown. The waves emitted at large x, i.e., at points more distant from the nanofocus, should be emitted significantly earlier to precompensate for the longer propagation times. They should also have different amplitudes due to the differences in A. Finally, there is clearly a negative chirp (gradual decrease of frequency with time). This is due to the fact that the higher frequency components propagate more slowly and therefore must be emitted earlier to form a coherent ultrashort pulse at the nanofocus.

In Figure 2.3(e), we display together all three of the representative waveforms at the thick edge to demonstrate their relative amplitudes and positions in time. The pulse at the extreme point in x (shown by blue) has the longest way to propagate and therefore is the most advanced in time. The pulse in the middle point (shown by green) is intermediate, and the pulse at the center ($x = 0$, shown by red) is last. One can notice also a counterintuitive feature: the waves propagating over longer trajectories are smaller in amplitude, although one may expect the opposite to compensate for the larger losses.

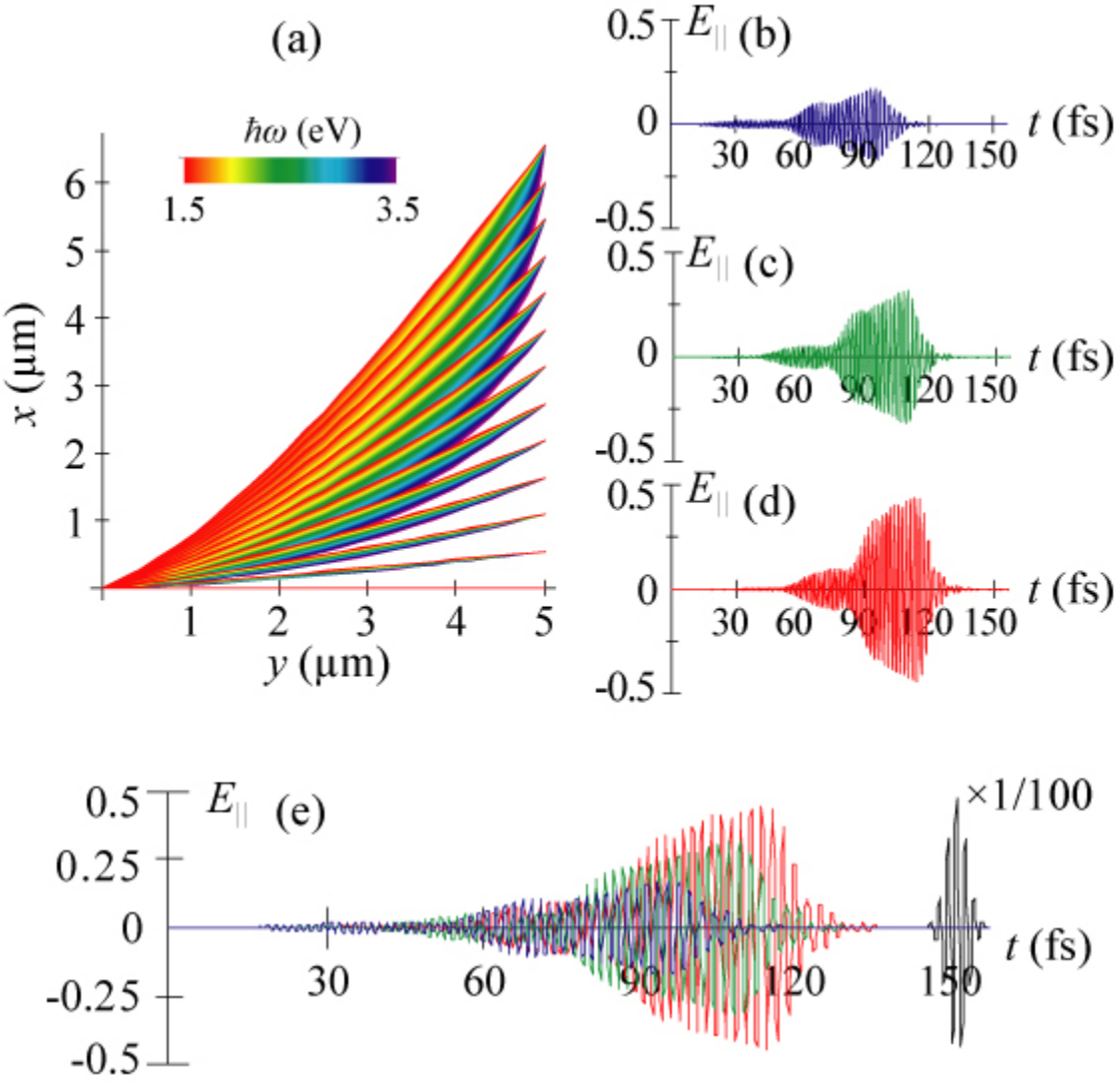

Figure 2.3. (color) (a) Trajectories (rays) of SPP packets propagating from the thick edge to the nanofocus displayed in the *xy* plane of the wedge. The frequencies of the individual rays in a packet are indicated by color as coded by the bar at the top. (b-d) Spatiotemporal modulation of the excitation pulses at the thick edge of the wedge required for nanofocusing. The temporal dependencies (waveforms) of the electric field for the phase-modulated pulses for three points at the thick edge boundary: two extreme points and one at the center, as indicated, aligned with the corresponding *x* points at panel (a). (e) The three excitation pulses of panels (b-d) (as shown by their colors), superimposed to elucidate the phase shifts, delays, and shape changes between these pulses. The resulting ultrashort pulse at the nanofocus is shown by the black line. The scale of the electric fields is arbitrary but consistent throughout the figure.

The explanation is that the losses are actually insignificant for the frequencies present in these waveforms, and the magnitudes are determined by the adiabatic concentration factor A.

Figure 2.3(e) also shows the resulting ultrashort pulse at the nanofocus. This is a transform-limited, Gaussian pulse. The propagation along the rays completely compensates for the initial phase and amplitude modulation, exactly as intended. As a result, the corresponding electric field of the waveform is increased by a factor of 100. Taking the other component of the electric field and the magnetic field into account, the corresponding increase of the energy density is by a factor $\sim 10^4$ with respect to that of the SPPs at the thick edge.

Consider the efficiency of the energy transfer to the nanoscale. This is primarily determined by the cross section σ_{SPP} for scattering of photons into SPPs. For instance, for a metal sphere of radius R at the surface of the wedge, one can obtain an estimate $\sigma_{SPP} \sim R^6 / \left(a_m^3 \lambda\right)$, where λ is the reduced photon wavelength. Setting $R \sim a_m$, we estimate $\sigma_{SPP} \sim 3\, nm^2$. Assuming optical focusing into a spot of $\sim 300\, nm$ radius, this yields the energy efficiency of conversion to the nanoscale of $\sim 10^{-3}$. Taking into account the adiabatic concentration of energy by a factor of 10^4, the optical field intensity at the nanofocus is enhanced by 1 order of magnitude with respect to that of the incoming optical wave.

The criterion of applicability of the WKB approximation is $\partial k^{-1} / \partial y << 1$. By substituting $k = k_0 n$ and Eq. (2.5), we obtain a condition $a_m / \left(n_{as} L\right) << 1$. This condition is satisfied everywhere including the nanofocus because $n_{as} \sim 1$ and $a_m << L$ for adiabatic grading. The minimum possible size of the wavepacket at the nanofocus in the direction of propagation, Δx,

is limited by the local SPP wavelength: $\Delta x \sim 2\pi / k \approx 2\pi a_f / n_{as}$. The minimum transverse size a (waist) of the SPP beam at the nanofocus can be calculated as the radius of the first Fresnel zone: $b = \pi / k_x \geq \pi / (k_0 n_x)$. Because n_x is constant along a trajectory, one can substitute its value at the thick edge (the launch site), where from Eq. (2.5) we obtain $n_x \approx n = n_{as} / a_m$. This results in $b \approx \pi a_m / n_{as}$; thus b is on order of the maximum thickness of the wedge, which is assumed also to be on the nanoscale.

2.5 Conclusions

To briefly conclude, we have proposed and theoretically investigated an approach to full coherent control of spatiotemporal energy localization on the nanoscale. From the thick edge of a plasmonic metal nanowedge, SPPs are launched whose phases and amplitudes are independently modulated for each constituent frequency of the spectrum and at each spatial point of the excitation. This premodulates the departing SPP wave packets in such a way that they reach the required point at the sharp edge of the nanowedge in phase, with equal amplitudes forming a nanofocus where an ultrashort pulse with required temporal shape is generated. This system constitutes a "nanoplasmonic portal" connecting the incident light field whose features are shaped on the microscale, with the required point or features at the nanoscale.

Chapter 3. Nanoconcentration in the Terahertz Frequency Region

3.1 Introduction to Terahertz (THz) Electromagnetics

Terahertz (THz) radiation ($1\,\mathrm{THz} = 10^{12}$ Hz) consists of electromagnetic waves with wavelengths between microwaves and mid-infrared. The THz region of the electromagnetic spectrum has been shown to be one of the most difficult to explore because of the lack of inexpensive and convenient sources, sensitive detectors and other components for the manipulation in this wavelength range [67]. Neither optical nor microwave techniques are directly applicable in the THz range. However, within the past 20 years, THz systems have undergone significant changes. This includes the creation of the new high-power sources and demonstration of remarkable applications of THz such as semiconductor and high-temperature superconductor characterization, label-free genetic analysis, cellular level and tomographic imaging and biological and chemical sensing [68-71]. The idea of using THz radiation for imaging and sensing is attractive because of the reduced scattering losses, which allow seeing through fog and detecting defects in optically opaque materials. Recently, this list of applications was expanded to include quality control, package inspection and non-destructive testing [72]. Most of these applications became possible because of the transparency of common package

materials in THz region and due to the fact that materials exhibit unique spectral fingerprints in the THz part of the spectrum.

In order to generate THz radiation several methods currently exist; for example, the photoconductive and electro-optic techniques. In the photoconductive approach, the resonant excitation of a semiconductor by a femtosecond laser is used, which generates current by the excitation of electrons and holes, leading to the creation of THz radiation [73]. In contrast to this resonant process, the electro-optic method is a non-resonant process which is based on the second-order susceptibility of the media with asymmetric unit cell. In this method, known also as optical rectification, a mixture of difference-frequency components add coherently to produce a pulse of THz radiation [74].

There are also two techniques for the detection of THz pulses: photoconductive sampling and free-space electro-optic sampling. Photoconductive detection is similar to photoconductive generation. Due to the shortness of the produced current pulse, the averaged current is measured, instead, as a function of the delay between the optical gate pulse and the THz pulse [75]. The electro-optics effect is the coupling of THz pulse and optical pulse in the sensor crystal. The THz electric field modulates the birefringence (double refraction) of the sensor crystal. This birefringence is tested by an optical probe beam as a function of the delay between the probe and the THz pulse [76].

THz spectroscopy is the combination of generation and detection techniques described above. It allows obtaining the optical properties of materials in the far-infrared region. There are several types of THz spectroscopy systems. The most recent technique is known as THz

time-domain spectroscopy (THz –TDS), in which sub-picosecond optical pulses are used to generate broadband THz radiation via a second-order nonlinear process. In such systems, both generation and detection of broadband THz radiation are obtained from a short optical pulse through non-linear interaction between the optical pulse and a medium [77]. TDS can provide the time-resolved phase information while conventional Fourier transform spectroscopy (FTS) is only sensitive to the amplitude [78].

3.2 Concentration of THz Fields

During the past decade, there were explosions in the research and development of nanoplasmonics in the visible and near-infrared (near-ir) frequency regions [32]. One of the most fundamental effects in nanoplasmonics is nanoconcentration of optical energy. Plasmonic nanofocusing has been predicted [40] and experimentally achieved [44, 45, 61]. Nanoconcentration of optical energy at nanoplasmonic probes made possible optical ultramicroscopy with nanometer-scale resolution [79-81] and ultrasensitive Raman spectroscopy [82]. It will be very beneficial for the fundamental science, engineering and environmental applications to be able to nanoconcentrate terahertz radiation with frequency $1-10\,\mathrm{THz}$ or vacuum wavelength $\lambda_0 = 300-30\,\mu m$. This will allow for nanoscale spatial resolution for THz imaging [83] and introduce THz spectroscopy on the nanoscale, taking full advantage of the rich THz spectra and submicron to nanoscale structures of many engineering, physical, and biological objects of wide interest: electronic components (integrated circuits, etc.), bacteria, their spores, viruses, macromolecules, carbon clusters and nanotubes, etc. There are existing approaches to

deep subwavelength THz imaging and probing based on sharp tips irradiated by a THz source [84], adiabatically-tapered metal-dielectric waveguides [85] and nonlinear microscopic THz sources [86]. For the development of the THz nanotechnology, it is extremely important to understand the limits to which the THz radiation energy can be concentrated spatially (nanofocused).

A major challenge for nanoconcentration of electromagnetic energy in the THz region is the large radiation wavelength in vacuum or conventional dielectrics $\lambda_0 = 30 - 300\ \mu m$, where the THz radiation can only be focused to the relatively very large regions of size $\sim \lambda_0 / 2$. The developed field of optical energy concentration, which is based on surface plasmon polaritons (SPPs), suggests that one of the ways to solving this problem is to employ the surface electromagnetic waves (SEWs). In the far-infrared, the dielectric permittivities of metals have large imaginary part which dominate over their negative real parts [87]. This implies that SEWs propagating along a metal-dielectric flat interface in this frequency range, known as Sommerfeld-Zenneck waves [38, 39], are weakly bound to the surface [88] and can hardly be used for the confinement of THz radiation.

It has been suggested that periodically perforating flat surfaces of ideal metals with grooves or holes leads to the appearance of SEWs, which mimic ("spoof") SPPs, that are more strongly bound to the surfaces [89-91], permitting better control over the THz fields. It has been predicted that SPPs on an array of parallel grooves cut on the surface of a perfect conductor wire can be localized by adiabatic deepening of the grooves [62]. At a point, where grooves are approximately a quarter of wavelength of light, the highest concentration is achieved to be on the

order of tens of micrometers. This method restricts the localization point to a particular frequency, making the concentration very narrow-band. Also, the depth of a groove should be $\sim \lambda_0 / 4$, i.e., in the tens to hundred micron range, which precludes completely nanoscale devices. The spoof plasmons will be discussed in detail in the next Chapter.

It is well known from microwave technology that the ideal-metal waveguides with smooth surfaces support TEM waves, where the electric field lines are either infinitely extended or terminate at the metal surfaces normally to them. The latter case requires the waveguide cross-section topology to be more than single-connected; an example may be a coaxial waveguide ("coax"). Such waveguides are very wide-band in frequency. The THz waveguides can be adiabatically tapered to concentrate energy. The idea of adiabatic energy concentration comes from ultramicroscopy [92-94] and nanoplasmonics [40], where it has been developed both theoretically and experimentally [44, 45, 61] and used in ultrasensitive surface enhanced Raman spectroscopy [82]. Employing the idea of adiabatic concentration and using a tapered metal-dielectric waveguide, the THz spatial resolution achieved is $\sim 20 \mu m$ across the entire THz spectrum [85].

In this Chapter, we establish the fundamental limits and find the principles of designing the optimum and efficient metal/dielectric nanowaveguides suitable for THz nanofocusing [95]. The specific examples are for the wide-band concentrators: a plasmonic metal wedge cavity and tapered coax waveguides, which are terminated by funnel-type adiabatic tapers. Such nanoconcentrators, along with the advent of high-power sources [96, 97] and sensitive detectors

[98] of THz radiation, will open up an extremely wide range of possible THz applications: material diagnostics, probe nanoimaging, biomedical applications, etc. – cf. [99-101].

Note that an alternative approach to THz energy concentration using doped semiconductor tapers has also been proposed [102]. However, the required heavy doping of the semiconductors may cause fast electron relaxation due to the collisions with the inflicted lattice defects and bring about high losses. Therefore, here we will pursue the adiabatic nanoconcentration of the THz radiation using metal/dielectric structures.

3.3 Principal Limits of Concentration of THz Radiation

Conventionally for THz and microwave regions, the metals are considered as ideal, which is equivalent to neglecting their skin depth

$$l_s = 1/\operatorname{Re}\kappa_m = \lambda\!\!\!^{-}_0 / \operatorname{Re}\sqrt{-\varepsilon_m}\ , \qquad (3.1)$$

where ε_m is the permittivity of the metal (we take into account that in the THz region $|\varepsilon_m| >> 1$), and $\lambda\!\!\!^{-}_0 = c/\omega$ is the reduced wavelength in vacuum. It is true that in the THz region $l_s = 30 - 60nm$, i.e. $l_s << \lambda_0 \approx 300\,\mu m$. However, as we show below, it is the finite skin depth, small as it is, that principally limits the ultimum localization size of the THz fields. For larger waveguides, the THz wave energy is localized mostly in the vacuum (dielectric) and its losses, which occur in the metal's skin layer, are correspondingly small. The effective quality factor (or, figure of merit) of the waveguide, which shows how many periods the wave can propagate without significantly losing its energy, can be estimated as

$$Q \sim 2a / l_s , \tag{3.2}$$

where a is the characteristic minimum size of the waveguide. This estimate becomes a good approximation for a metal-dielectric-metal (MIM) planar waveguide [see below Eq. (3.4)]. When the waveguide size reduces to become on the order of the skin depth, $a \le l_s$, the THz field is pushed into the metal, and the quality factor is reduced to $Q \le 1$, which implies strong losses.

Qualitatively, this establishes the limit to the nanoconcentration: for the upper THz region $a \ge l_s \approx 30nm$, while for the 1 THz frequency $a \ge l_s \approx 60nm$. These are the practical limits of the THz nanoconcentration for the noble metals (silver, gold, and platinum) and for aluminum.

If one pursues the goal of creating enhanced local fields in a small region, but not necessarily to efficiently transfer the THz energy from the far field to the near field, then the apertureless SNOM approach, where a sharp metal or dielectric tip is irradiated by THz radiation, can, in principle, achieve even higher resolution [103]. However, the efficiency of utilizing the THz energy of the source in this case will be extremely low; the stray, far-field THz energy may create a significant parasitic background.

Below, we consider examples of the THz adiabatic nanoconcentration quantitatively, where the effect of the specific geometry will become apparent.

3.4 Fundamental Mode in MIM Waveguides at Low Frequencies

Consider first a parallel plate waveguide that consists of a dielectric slab of thickness a with dielectric permittivity ε_d sandwiched between two thick metal plates (with thickness of at least a few l_s (Eq. (3.1)), i.e., greater than 200 nm in practical terms) [see Figure 3.1(a)].

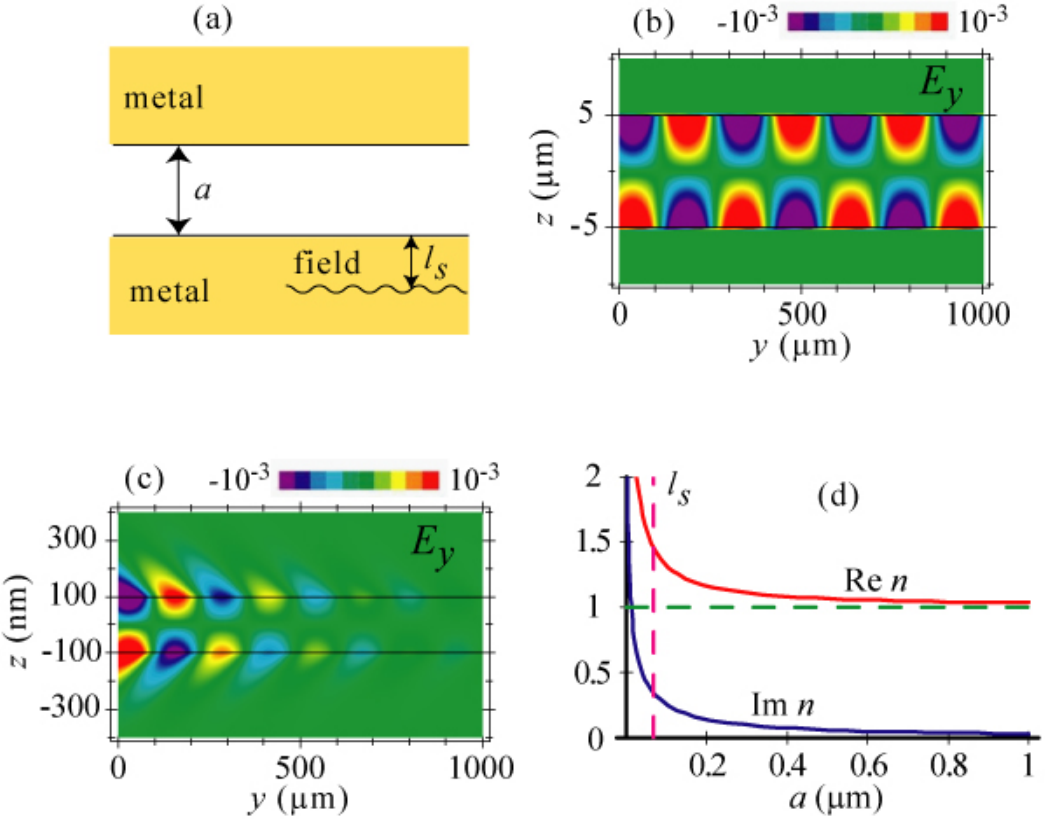

Figure 3.1. (color) (a) Schematic of the waveguide. The width of the dielectric gap a and the skin depth l_s are indicated. (b) An instantaneous distribution of the longitudinal electric field E_y along the propagation coordinate y for $a = 10\,\mu m$ and frequency 1 THz in a silver-vacuum-silver waveguide. (c) The same as in panel (b) but for $a = 200\,nm$. (d) Modal refraction index $n = k / k_0$ ($\mathrm{Re}\,n$ is denoted by the red line and $\mathrm{Im}\,n$ by the blue line) as a function of the waveguide width a. Dashed green line indicates the value of n for the perfect conductor. Skin depth value is shown by the vertical dashed line.

The permittivity of the metal ε_m in the THz region has a very large ($\geq 10^6$) imaginary part that defines the very small skin depth $l_s \leq 100\,nm$, which justifies the usual consideration of the metals as perfect conductors [87].

However, as we have already mentioned, for our purposes of THz nanoconcentration, we need to take into account the field penetration into the metal, i.e., its finite skin depth. Inside the metal, this THz field drives the oscillations of the metal conduction electrons, which is by definition a plasmonic effect. This is accompanied, in particular, by the THz energy loss that limits the THz energy concentration. In this case the propagating modes of the system are SPPs, which are TM modes characterized by symmetry with respect to the reflection in the center plane. We will orient the coordinate system with its z axis normal to the plane and the y axis in the direction of propagation. The symmetric (even) modes have even field components H_x and E_z and odd E_y; the parity of the antisymmetric (odd) modes is opposite, and their properties are described in Subsection 1.3.2.

From plasmonics it is known that the even modes have a larger fraction of their energy localized in the dielectric and the odd modes in the metal. Therefore, the even modes have much smaller damping and are most suitable for the THz energy concentrations (see Subsection 1.3.2). The dispersion relation for the even modes is given by equation (1.35).

In the terhertz range ε_m is mainly imaginary, i.e. $\mathrm{Im}\,\varepsilon_m >> 1$. Consequently, $\kappa_m \approx k_0\sqrt{-\varepsilon_m} = l_s^{-1}(1-i)$, where $l_s = (1-i)/(k_0\sqrt{-i|\varepsilon_m|}) = \sqrt{2}/(k_0\sqrt{|\varepsilon_m|})$ is the metal skin depth (see also Eq. (3.1)), which is on the order of tens of nanometers. We also assume that

$\kappa_d a << 1$, which is always the case for the mode under consideration because either this mode is close to the TEM mode where $k = k_0\sqrt{\varepsilon_d}$, or the gap a is thin enough. This leads to a closed expression for the index of refraction of the mode. From Eq. (1.35) under the conditions that $\kappa_d a << 1$ and $\mathrm{Im}\,\varepsilon_m >> 1$, we obtain

$$\frac{1}{2}k_0 a\sqrt{n^2-\varepsilon_d} = \frac{\varepsilon_d}{\sqrt{-\varepsilon_m}\sqrt{n^2-\varepsilon_d}}. \tag{3.3}$$

Therefore, the index of refraction takes the following form:

$$n = \sqrt{\varepsilon_d}\left(1+\frac{2}{k_0 a\sqrt{-\varepsilon_m}}\right)^{1/2} = \sqrt{\varepsilon_d}\left(1+\frac{l_s(i+1)}{a}\right)^{1/2} \approx \sqrt{\varepsilon_d}\left(1+i\frac{l_s}{2a}\right). \tag{3.4}$$

where the approximate equality is valid for not too tight nanofocusing, i.e., for $l_s << a$. Using this, one can check that $\kappa_d a \approx \left(\varepsilon_d a l_s / \lambda\!\!\!^{-2}_0\right)^{1/2}$. Consequently, the applicability condition of the approximation used is

$$\left(\varepsilon_d a l_s / \lambda\!\!\!^{-2}_0\right)^{1/2} << 1. \tag{3.5}$$

This condition is satisfied for the realistic parameters of the problem. For instance, for the frequency $f = 1\,THz$, the skin depth for metals is $l_s \approx 60\,nm$, while the reduced wavelength is $\lambda\!\!\!^{-}_0 \approx 75\,\mu m$. The condition Eq. (3.5) is well satisfied for $a << 100\,\mu m$, i.e., in the entire range of interest to us. From Eq. (3.4), we can obtain the quality factor of the waveguide $Q = \mathrm{Re}\,n / \mathrm{Im}\,n = 2a / l_s$, giving a quantitative meaning to the estimate Eq. (3.2).

Plasmonic effects (i.e. those of the finite skin depth l_s) are illustrated in Figure 3.1 for silver-vacuum-silver waveguide and frequency of 1 THz. Figure 3.1(b) and (c) display the longitudinal electric field E_y from Eq. (1.27), which is the exact solution of the Maxwell

equations. Note that this field component is absent for the ideal conductor; here it is relatively small, on the order of 10^{-3} of the transverse field. Figure 3.1(b) illustrates the case of a relatively wide waveguide ($a = 10\,\mu m$), where it is evident that the electric field is localized mostly in the dielectric region of the waveguide, and the extinction of the wave is small. In a sharp contrast, for a nanoscopic waveguide ($a = 200\,nm$) in Figure 3.1(c), the electric field significantly penetrates the metal. In accord with our arguments, there is a very significant extinction of the fields as they propagate; the retardation effects are also evident: the lines of equal amplitude are at an angle relative to the normal z direction. The dependence of the modal refraction index on the thickness a of the waveguide obtained from Eq. (3.4) is plotted in Figure 3.1(d). This index increases as a becomes comparable with the skin depth. While $\mathrm{Re}\,n$ and $\mathrm{Im}\,n$ increase by the same absolute amount, the quality factor Q, obviously, greatly decreases with decrease of a. Such mode described above can be used for broadband energy concentration of THz waves.

3.5 Concentration of Terahertz Fields on Wedge

3.5.1 Straight Wedge

To introduce the THz nanoconcentration, consider a metal-dielectric-metal waveguide that is slowly (adiabatically) tapered off as a wedge, as illustrated in Figure 3.2(a). Because of the adiabatic change of the parameters, a wave propagating in such a waveguide will adjust to it without reflection or scattering, just as it takes place in nanoplasmonic waveguides [40].

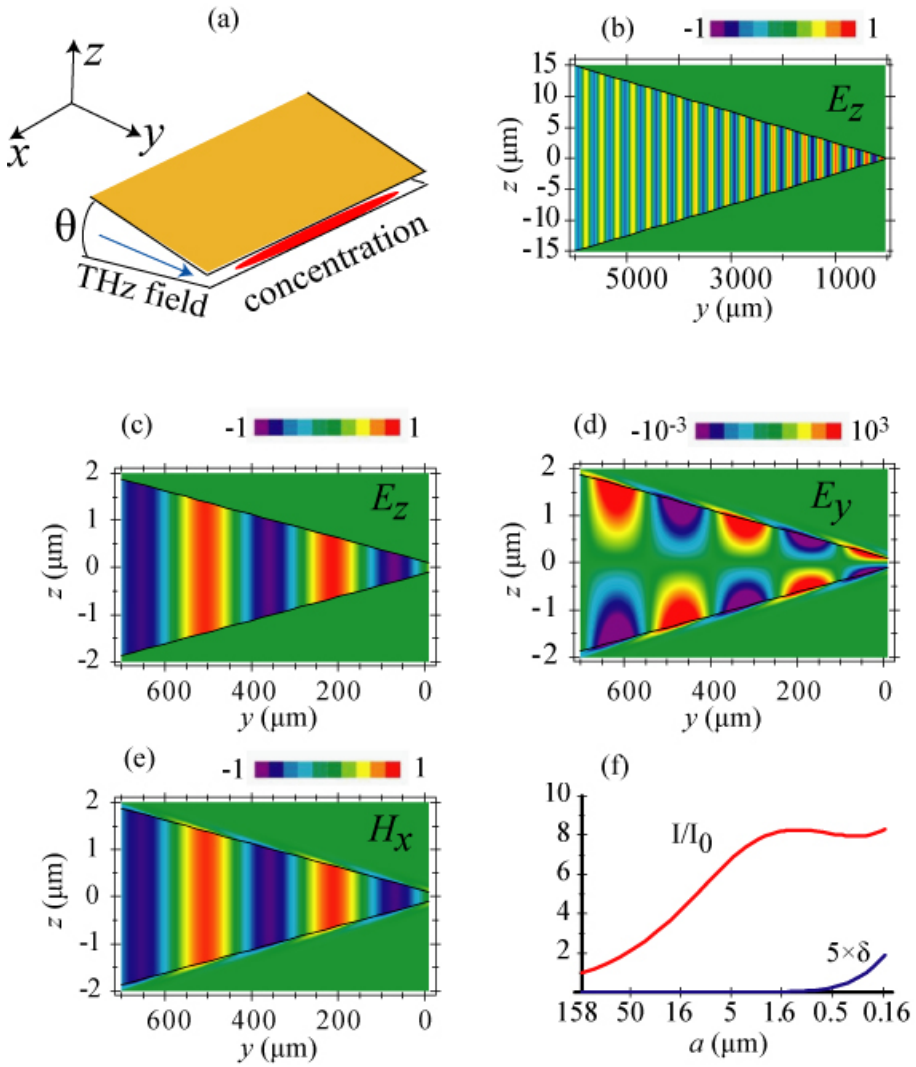

Figure 3.2. (color) (a) Schematic of energy concentration, where θ is the wedge opening angle, the arrow indicates the direction of propagation of the THz wave, and the red highlights the area of the adiabatic concentration. (b) An instantaneous distribution of the transverse electric field E_z of the THz wave propagating and concentrating along the wedge waveguide for the last 6 mm of the propagation toward the edge. (c) An instantaneous spatial distribution of the transverse electric field E_z for the last $700\,\mu m$ of the propagation. (d) The same as (c) but for E_y. (e) The same as (c) but for the H_x. (f) Dependence of THz field intensity in the middle of waveguide on the dielectric gap width a (the red line). The blue curve displays the dependence on a of the adiabatic parameter δ, scaled by a factor of 5. The values of a indicated at the successive horizontal axis ticks differ by a factor of $10^{-1/2}$, i.e., by 5 dB.

As a result, propagating it will concentrate its energy, conforming to the tapering of the waveguide.

The corresponding solution can be obtained from the Maxwell equations using the Wentzel-Kramers-Brillouin (WKB) approximation (see Section 1.4), similarly to the nanoplasmonic case in the visible part of the spectrum. The WKB approximation is applicable under the conditions that

$$\delta = \left| d(\mathrm{Re}\, k^{-1}) / dy \right| << 1 \quad \text{and} \quad \left| da / dy \right| << 1 . \tag{3.6}$$

where δ is the adiabatic parameter describing how slowly the modal wavelength changes on a distance of its own, and $\left| da / dy \right|$ is a parameter describing how adiabatically the transverse size of the confined mode changes along the propagation coordinate.

The phase of the mode (eikonal) is given by the following integral (Eq. (1.37)):

$$\Phi(y) = k_0 \int n(y) dy , \tag{3.7}$$

where $n(y)$, defined by Eq. (3.4), is the local index of the mode. The behavior of the wave amplitude as a function of the propagation coordinate *y* is found from the condition of flux conservation:

$$J(y) = v_g(y) \int_{-\infty}^{\infty} W(y,z) dz = const . \tag{3.8}$$

Here $v_g(y) = \partial\omega / \partial k$ is the wave local group velocity, and $W(y,z)$ is energy density in the mode, which is given by Eq. (2.7). The energy density $W(y,z)$ can be derived using the fields in Eqs (1.26)-(1.28) and proceeding similar to the derivation of Eq. (2.8); it takes the following form

$$W=\frac{1}{4\pi}\begin{cases}\left(\dfrac{\partial(\omega\,\mathrm{Re}\,\varepsilon_m)}{\partial\omega}\dfrac{|k|^2+|\kappa_m|^2}{k_0^2\varepsilon_m}+1\right)e^{-2\mathrm{Re}\,\kappa_m(z-a/2)}, & \mathrm{z}>\mathrm{a}/2\\ \dfrac{|k\sinh(\kappa_d z)|^2+|\kappa_d\cosh(\kappa_d z)|^2}{|\varepsilon_d|k_0^2|\cosh\left(\kappa_d\dfrac{a}{2}\right)|^2}+\dfrac{|\sinh(\kappa_d z)|^2}{\left|\cosh\left(\kappa_d\dfrac{a}{2}\right)\right|^2}, & |\mathrm{z}|<\mathrm{a}/2\,.\\ \left(\dfrac{\partial(\omega\,\mathrm{Re}\,\varepsilon_m)}{\partial\omega}\dfrac{|k|^2+|\kappa_m|^2}{k_0^2\varepsilon_m}+1\right)e^{2\mathrm{Re}\,\kappa_m(z+a/2)}, & \mathrm{z}<-\mathrm{a}/2\end{cases} \tag{3.9}$$

By integrating Eq.(3.9) over z, we obtain the expression for the flux:

$$J(y)=\frac{\partial\omega}{\partial k(y)}\left\{\begin{array}{l}\dfrac{1}{\mathrm{Re}\,\kappa_m}\left(\dfrac{\partial(\omega\,\mathrm{Re}\,\varepsilon_m)}{\partial\omega}\dfrac{|k|^2+|\kappa_m|^2}{k_0^2|\varepsilon_m|^2}+1\right)e^{\mathrm{Re}\,\kappa_m a}+\\ +\dfrac{1}{|\varepsilon_d|k_0^2|\cosh(\kappa_d a/2)|^2}\left[\dfrac{|k|^2+|\kappa_d|^2}{2\,\mathrm{Re}\,\kappa_d}\sinh(\mathrm{Re}\,\kappa_d a)\right.\\ \left.-\dfrac{|k|^2-|\kappa_d|^2}{2\,\mathrm{Im}\,\kappa_d}\sin(\mathrm{Im}\,\kappa_d a)\right]+\\ +\dfrac{1}{2|\sinh(\kappa_d a/2)|^2}\left[\dfrac{\sinh(\mathrm{Re}\,\kappa_d a)}{\mathrm{Re}\,\kappa_d}-\dfrac{\sin(\mathrm{Im}\,\kappa_d a)}{\mathrm{Im}\,\kappa_d}\right]\end{array}\right\}. \tag{3.10}$$

Since during the concentration the flux should be conserved, this equation provides the normalization coefficients for the fields Eqs.(1.26)-(1.28).

Turning to the concentration, the behavior of the dominant transverse field component E_z as a function of the coordinate *y* along the propagation direction is shown for the last 6 mm of the propagation toward the edge in Figure 3.2(b). There is a clearly seen spatial concentration of the energy and increase of the field as the wave is guided into the taper. The predicted behavior of the two components of electric field and the magnetic field for the last $700\,\mu m$ of the propagation is shown in Figure 3.2(c)-(e). They indicate that the adiabatic concentration occurs

without an appreciable loss of the intensity. The THz wave follows the waveguide up to the nanometric size.

The red line in Figure 3.2(f) shows that the local intensity I as the function of the thickness a of the waveguide for $a < 4\,\mu\text{m}$ increases significantly with $1/a$, in qualitative accord with the behavior expected for the negligibly low losses. This intensity reaches its maximum for $a = 1.6\,\mu\text{m}$ and then starts to decrease as the losses overcome the adiabatic concentration. At smaller thicknesses, $a \le 400\,n\text{m}$, the intensity in Figure 3.2(f) starts to increase again, which is unphysical. The reason is revealed by the behavior of the adiabatic parameter δ shown by the blue line: for $a \le 400\,n\text{m}$, δ becomes relatively large (comparable with 1), i.e., the adiabaticity is violated. This is due to the fact that the fraction of the THz field energy propagating in the metal is dramatically increased for $a \le 400\,n\text{m}$ due to the constricted transverse extension of the dielectric in the waveguide. This causes a significant loss per wavelength λ, leading to a rapid change of the wave vector k, breaking down the adiabaticity. This constitutes a fundamental difference from the nanoplasmonic adiabatic concentration in the optical region where the adiabatic parameter is constant, and the adiabaticity holds everywhere including the vicinity of the tip [40].

3.5.2 Advantages of an Elongated Wedge

To provide for the optimum guiding of the THz wave and its concentration on the nanoscale, the terminating (nanoscopic) part of the waveguide should be tapered slowly, in a funnel-like manner. That is, one needs to decrease the grading da/dy of the waveguide near the edge in

order to keep the adiabaticity parameter $\delta = \left| d(\mathrm{Re}\, k^{-1}) / da \times da / dy \right|$ approximately constant and small enough to prevent back-reflection. Because for the adiabatic grading (tapering), the derivative $d(\mathrm{Re}\, k^{-1}) / da$ does not depend on the grading (it is the same as for the plane waveguide) and is only a function of a, the equation $\delta = \delta(y)$ is a differential equation for the shape of the waveguide that can be easily integrated. This results in the dependence of the thickness a on the longitudinal coordinate y determined by a simple integral

$$\mathrm{Re}\, n^{-1}(a) = k_0 \int \delta(y) dy \,. \tag{3.11}$$

where $n(a)$ is the modal index defined in this case by Eq. (3.4), and $\delta(y)$ is the desired dependence of the adiabatic parameter along the waveguide, which is an arbitrary function of y satisfying the adiabaticity conditions, Eq. (3.6).

The geometry of an adiabatically-tapered end of the silver/vacuum waveguide found from Eq. (3.11) and satisfying Eq. (3.6) and the corresponding WKB solutions for the 1 THz fields are shown in Figure 3.3(a)-(c). The optimum shape of the waveguide in this case is funnel-like, greatly elongated toward the edge. The nanoconcentration of the field is evident in Figure 3.3(a)-(c), as well as its penetration into the metal for $a \le 100\, n\mathrm{m}$. As these panels show quantitatively and the red curve on Figure 3.3(d) summarizes, the field intensity reaches its maximum at $a \approx 300\, n\mathrm{m}$ where it is enhanced with respect to the field at the entrance to the funnel waveguide by a modest factor of 1.2. At the same time, the adiabatic parameter δ decreases toward the tip from 0.07 to 0.05, indicating the applicability of the WKB approximation everywhere.

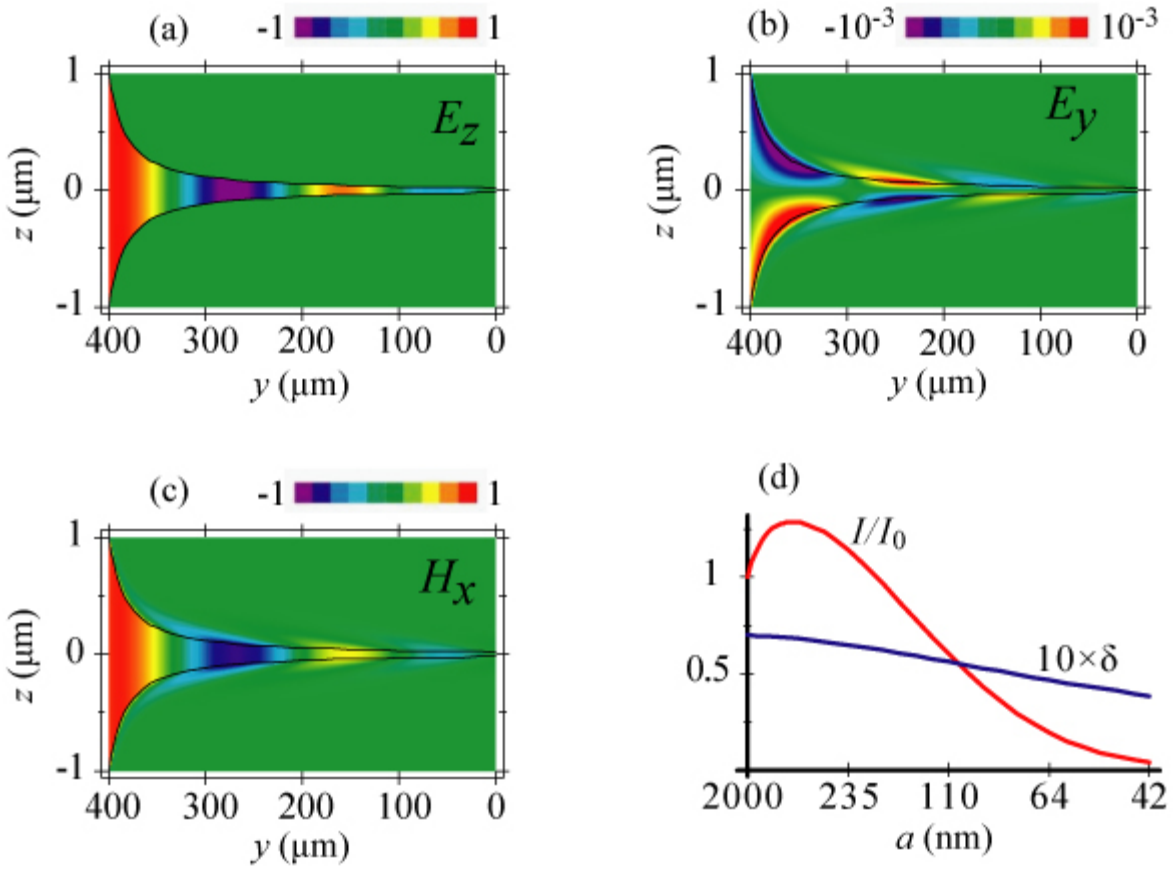

Figure 3.3. (color) Terahertz energy concentration in adiabatically tapered curved-wedge waveguide. (a) Instantaneous distribution of the transverse component of the THz electric field E_z (in the central plane $z = 0$) as a function of the coordinate y along the propagation direction for the last $400\ \mu m$ of the propagation. (b) The same as in panel (a) but for the longitudinal electric field component E_y (c) The same as panel (a) but for the transverse magnetic field H_x. The units for the fields are arbitrary but consistent between the panels. (d) The THz field intensity I (relative to the intensity I_0 at the entrance of the waveguide) as a function of the dielectric gap thickness a is shown by the red line. The adiabatic parameter scaled by a factor of 10 as a function of a is indicated by the blue line. The values of a indicated at the horizontal axis ticks correspond to the values of y at the ticks of panels (a)-(c).

Note that this funnel-shaped wedge, indeed, continues the linearly-graded wedge waveguide shown in Figure 3.2, which yields an enhancement factor of ≈ 8 at $a = 2\ \mu m$. Sequentially,

these two waveguides provide an intensity enhancement of approximately $\times 10$ while compressing the THz wave to the thickness of $a = 300\,n\text{m}$, and an enhancement by a factor of 3 for $a = 100\,n\text{m}$.

To conclude, true nanolocalization of THz radiation in one dimension (1d) is possible. The minimum transverse size of this nanolocalization is determined by the skin depth, as we have already discussed qualitatively in Section 3.3. The obtained 1d beam of the nanoconcentrated THz radiation may be used for different purposes, in particular as a source for the diffraction elements including the nanofocusing zone plates of the type introduced in [104].

3.6 Concentration on a Coaxial Cable

3.6.1 Fundamental Mode in a Coaxial Cable

The two-dimensional (2d) concentration of the THz radiation can be achieved by using an adiabatically-tapered conical coax waveguide. Before considering the concentration for the THz frequencies on the coaxial cable, we obtain the useful equation for the mode that is supported in such structures.

To get the wave equation, one should use the Maxwell's equations (1.1)-(1.6). Eliminating the electric field $\mathbf{E}$ from these equations and using the fact that $\nabla \times \nabla \times \mathbf{H} = \nabla(\nabla \cdot \mathbf{H}) - \nabla^2 \mathbf{H}$, we reach the wave equation for homogeneous medium with constant ε:

$$\nabla^2 \mathbf{H} - \frac{\varepsilon}{c^2} \frac{\partial^2 \mathbf{H}}{\partial t^2} = 0\,. \tag{3.12}$$

The magnetic field in cylindrical coordinate system (ρ,φ,y) has only a $\varphi-$component, since we are interested in TM mode. We can also assume that derivatives with respect to φ are zero because the field is azimuthally uniform. Therefore, the wave equation (3.12) in cylindrical coordinates is

$$\frac{\partial^2 H_\varphi}{\partial y^2}+\frac{\partial}{\partial\rho}\left(\frac{1}{\rho}\frac{\partial}{\partial\rho}\left(\rho H_\varphi\right)\right)-\frac{\varepsilon}{c^2}\frac{\partial^2 H_\varphi}{\partial t^2}=0\,. \tag{3.13}$$

The differential equation (3.13) is commonly solved by the technique of separation of variables. The basic idea behind this technique is to assume, initially, that the variable of interest can be separated into factors which depend separately on the coordinates. In this case, we set that H_φ can be expressed as

$$H_\varphi=R(\rho)Y(y)T(t). \tag{3.14}$$

Substitution of (3.14) into (3.13) and division of the result by (3.14) yields

$$\frac{1}{Y(y)}\frac{\partial^2 Y}{\partial y^2}+\frac{1}{R(\rho)}\left(\frac{\partial^2 R}{\partial\rho^2}+\frac{1}{\rho}\frac{\partial R}{\partial\rho}-\frac{1}{\rho^2}R\right)-\frac{1}{T(t)}\frac{\varepsilon}{c^2}\frac{\partial^2 T}{\partial t^2}=0\,. \tag{3.15}$$

Note that each of the terms is a function of different variables; thus, each of them must be constant:

$$\frac{1}{R(\rho)}\left(\frac{\partial^2 R}{\partial\rho^2}+\frac{1}{\rho}\frac{\partial R}{\partial\rho}-\frac{1}{\rho^2}R\right)=\kappa^2\,, \tag{3.16}$$

$$\frac{1}{Y(y)}\frac{\partial^2 Y}{\partial y^2}=-k^2\,,$$

$$\frac{\varepsilon}{T(t)c^2}\frac{\partial^2 T}{\partial t^2}=-k_0^2\varepsilon\,,$$

where $\kappa^2=k^2-k_0^2\varepsilon$. Each of these equations has a solution in terms of known functions:

$$R(\rho) = A_1 I_1(\kappa\rho) + A_2 K_1(\kappa\rho), \tag{3.17}$$

$$Y(y) = e^{iky},$$

$$T(t) = e^{-i\omega t},$$

where $I_1(\kappa\rho)$ and $K_1(\kappa\rho)$ are modified Bessel functions of the first and second kind, respectively. Here we choose the solution that corresponds to a wave propagating to the right. Physical fields must be real, therefore, one should take real part of this solution.

Now let us turn back to our system, which is a coaxial cable that has inner radius r and outer radius $R = r + a$, where a is the dielectric gap width. In each medium the solution should be selected in such way that it is not diverging at zero and infinity. Consequently, fields are described by equations

$$H_\varphi = A\, e^{i(ky-\omega t)} \begin{cases} BI_1(\kappa_m\rho) & \text{for } \rho < r \\ I_1(\kappa_d\rho) + CK_1(\kappa_d\rho) & \text{for } r < \rho < \mathrm{R}, \\ DK_1(\kappa_m\rho) & \text{for } \rho > \mathrm{R} \end{cases} \tag{3.18}$$

$$E_y = -\frac{\partial_\rho(\rho H_\varphi)}{ik_0\varepsilon_i\rho} = A\, e^{i(ky-\omega t)} \begin{cases} B\dfrac{i\kappa_m}{k_0\varepsilon_m} I_0(\kappa_m\rho) & \text{for } \rho < r \\ \dfrac{i\kappa_d}{k_0\varepsilon_d}\left(I_0(\kappa_d\rho) - CK_0(\kappa_d\rho)\right) & \text{for } r < \rho < \mathrm{R}, \\ -D\dfrac{i\kappa_m}{k_0\varepsilon_m} K_0(\kappa_m\rho) & \text{for } \rho > \mathrm{R} \end{cases} \tag{3.19}$$

$$E_\rho = \frac{\partial_y(H_\varphi)}{ik_0\varepsilon_i} = A\frac{k}{k_0} e^{i(ky-\omega t)} \begin{cases} BI_1(\kappa_m\rho)/\varepsilon_m & \text{for } \rho < r \\ \left(I_1(\kappa_d\rho) + CK_1(\kappa_d\rho)\right)/\varepsilon_d & \text{for } r < \rho < \mathrm{R}. \\ DK_1(\kappa_m\rho)/\varepsilon_m & \text{for } \rho > \mathrm{R} \end{cases} \tag{3.20}$$

From the boundary conditions of the continuity of the tangential components of the fields H_φ and E_y at the interfaces, we obtain the set of equations

$$BI_1(\kappa_m r) = I_1(\kappa_d r) + CK_1(\kappa_d r) \tag{3.21}$$

$$DK_1(\kappa_m R) = I_1(\kappa_d R) + CK_1(\kappa_d R),$$

$$B\frac{\varepsilon_d \kappa_m}{\varepsilon_m \kappa_d} I_0(\kappa_m r) = I_0(\kappa_d r) - CK_0(\kappa_d r)\ ,$$

$$-D\frac{\varepsilon_d \kappa_m}{\varepsilon_m \kappa_d} K_0(\kappa_m R) = I_0(\kappa_d R) - CK_0(\kappa_d R).$$

From the first and the third equations of (3.21) the constant C is

$$C = \frac{\dfrac{I_0(\kappa_d r)}{I_0(\kappa_m r)} - \dfrac{\varepsilon_d \kappa_m}{\varepsilon_m \kappa_d}\dfrac{I_1(\kappa_d r)}{I_1(\kappa_m r)}}{\dfrac{K_0(\kappa_d r)}{I_0(\kappa_m r)} + \dfrac{\varepsilon_d \kappa_m}{\varepsilon_m \kappa_d}\dfrac{K_1(\kappa_d r)}{I_1(\kappa_m r)}}. \tag{3.22}$$

Doing the same operation with the second and the fourth equations, the coefficient C becomes:

$$C = \frac{\dfrac{I_0(\kappa_d R)}{K_0(\kappa_m R)} + \dfrac{\varepsilon_d \kappa_m}{\varepsilon_m \kappa_d}\dfrac{I_1(\kappa_d R)}{K_1(\kappa_m R)}}{\dfrac{K_0(\kappa_d R)}{K_0(\kappa_m R)} - \dfrac{\varepsilon_d \kappa_m}{\varepsilon_m \kappa_d}\dfrac{K_1(\kappa_d R)}{K_1(\kappa_m R)}}. \tag{3.23}$$

Therefore, the characteristic relation for the TM mode of this coaxial waveguide is

$$\left(\frac{I_0(\kappa_d r)}{I_0(\kappa_m r)} - \xi\frac{I_1(\kappa_d r)}{I_1(\kappa_m r)}\right)\left(\frac{K_0(\kappa_d R)}{K_0(\kappa_m R)} - \xi\frac{K_1(\kappa_d R)}{K_1(\kappa_m R)}\right) = \left(\frac{K_0(\kappa_d r)}{I_0(\kappa_m r)} + \xi\frac{K_1(\kappa_d r)}{I_1(\kappa_m r)}\right)\left(\frac{I_0(\kappa_d R)}{K_0(\kappa_m R)} + \xi\frac{I_1(\kappa_d R)}{K_1(\kappa_m R)}\right). \tag{3.24}$$

where $\xi = \dfrac{\varepsilon_d \kappa_m}{\varepsilon_m \kappa_d}$. This equation is quadratic with respect to ξ and can be written in the form $\alpha\xi^2 + \beta\xi + \gamma = 0$, where the coefficients α, β and γ can be found as combinations of the Bessel functions by comparison to Eq. (3.24) (see Appendix). It can obviously be resolved for ξ yielding

$$\frac{\beta \pm \sqrt{\beta^2 - 4\alpha\gamma}}{2\alpha} = -\xi = -\frac{\varepsilon_d \kappa_m}{\varepsilon_m \kappa_d}. \tag{3.25}$$

In the THz region, only the mode with the minus sign in Eq. (3.25) propagates. Eq. (3.25) can be expanded over the small parameter $\kappa_d a << 1$ (a more detailed derivation is given in the Appendix) leading to

$$\frac{\kappa_d a}{\frac{K_0(\kappa_m R)}{K_1(\kappa_m R)} + \frac{I_0(\kappa_m r)}{I_1(\kappa_m r)}} = -\frac{\varepsilon_d \kappa_m}{\varepsilon_m \kappa_d}. \tag{3.26}$$

Since ε_m for THz frequencies is large and predominantly imaginary, we have $\kappa_m \approx k_0 \sqrt{-\varepsilon_m} = l_s^{-1}(1-i)$ and Eq. (3.26) simplifies to

$$n = \sqrt{\varepsilon_d}\left(1 + \left(\frac{K_0(\kappa_m R)}{K_1(\kappa_m R)} + \frac{I_0(\kappa_m r)}{I_1(\kappa_m r)}\right)\frac{l_s(1+i)}{2a}\right)^{1/2}. \tag{3.27}$$

where l_s is the metal skin depth. Similar to the wedge waveguide case, the applicability of this solution is given by Eq. (3.5).

When the arguments of the Bessel functions in Eq. (3.27) are large, i.e. $\kappa_m R >> 1$ and $\kappa_m r >> 1$, we can use asymptotics for Bessel functions $I_\nu(z) \approx \frac{e^z}{\sqrt{2\pi z}}\left(1 - \frac{4\nu^2 - 1}{8z} + O\left[\frac{1}{z^2}\right]\right)$ and $K_\nu(z) \approx \sqrt{\frac{\pi}{2z}} e^{-z}\left(1 + \frac{4\nu^2 - 1}{8z} + O\left[\frac{1}{z^2}\right]\right)$. Consequently,

$$\frac{K_0(\kappa_m R)}{K_1(\kappa_m R)} + \frac{I_0(\kappa_m r)}{I_1(\kappa_m r)} \approx 2 + \frac{1}{4\kappa_m}\left(\frac{1}{R} - \frac{1}{r}\right). \tag{3.28}$$

Therefore, the dispersion relation in this case becomes

$$n \approx \sqrt{\varepsilon_d}\left(1 + \left(2 + \frac{l_s(1+i)}{8}\left(\frac{1}{R} - \frac{1}{r}\right)\right)\frac{l_s(1+i)}{2a}\right)^{1/2} = \sqrt{\varepsilon_d}\left(1 + \frac{l_s(1+i)}{a} - \frac{l_s^2 i}{16rR}\right)^{1/2}, \tag{3.29}$$

which is consistent with Eq. (3.4) for the modal reflection index of the wedge.

3.6.2 Concentration Using a Tapered Coaxial Cable

In order to concentrate the THz radiation, we applied WKB approximation to the considered coaxial cable. The eikonal is determined by Eq. (3.7), where n is given by Eq. (3.27). The fields (3.18)-(3.20) also should be normalized so that energy flux J (through the plane $y = y_0$) is constant, i.e.

$$J(y_0) = 2\pi v_g(y_0)\int_0^\infty W(\rho, y_0)\rho d\rho = const\,. \tag{3.30}$$

where the energy density $W(\rho, y_0)$ is determined by Eq. (2.7) with the fields (3.18)-(3.20) and $v_g(y_0)$ is the group velocity. In this situation, $v_g(y_0)$ is equal to

$$v_g(y_0) = \frac{1}{\partial(k_0 n)/\partial\omega} = \left(\frac{n}{c} + k_0 \frac{\partial n}{\partial l_s}\frac{\partial l_s}{\partial \omega}\right)^{-1}. \tag{3.31}$$

where l_s is the metal skin depth, which depends on metal dielectric function, described by Drude equation (1.20) with parameters ω_p and Γ that are selected to fit experimental data [87].

Now let us discuss the numerical results for the theory described above. The geometry needed for concentration is illustrated in Figure 3.4(a). Calculated from the expression (3.27), the dependence of the modal refractive index $n = k(a, r)/k_0$ on the dielectric gap a is displayed in Figure 3.4(b) for the frequency of 1 THz, silver as a metal, and vacuum in the dielectric gap. The results are shown for two values of the radius of the central wire: $r = 10\,\mu$m and $r = 60\,n$m.

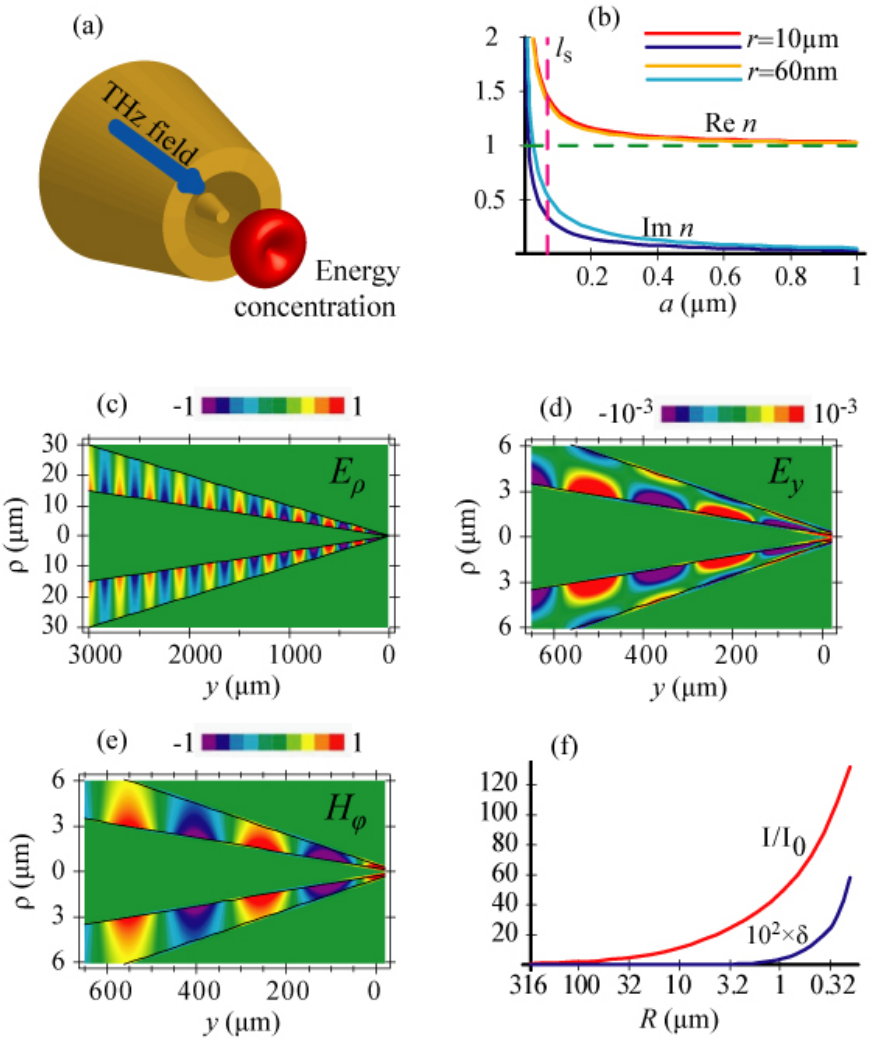

Figure 3.4. (color) (a) Schematic of geometry and energy concentration. (b) Dependence of modal refraction index n in coaxial waveguide on the dielectric gap width a for two central wire radii: $r = 10\,\mu m$ and $r = 60\,nm$ and $\varepsilon_d = 1$. (c) Instantaneous distribution of the radial THz electric field amplitude E_ρ in the cross section of the coax for the last $3\,mm$ of the propagation toward the tip. The amplitude of the field is color coded by the bar at the top of the panel. (d) Instantaneous distribution of the THz electric field amplitude E_y on the coordinate y for the last $650\,\mu m$ of the propagation. (e) The same as (d) but for the magnetic field H_φ. (f) Dependence of THz field intensity in the middle of the waveguide gap on the waveguide outer radius $R = r + a$ is shown in red. The blue curve displays the adiabatic parameter δ as a function of R, scaled by a factor of 10^2. The values of R indicated at the successive horizontal axis ticks differ by a factor of $10^{-1/2}$, i.e., by $5\,dB$.

As one can see from Figure 3.4(b), the real part of the modal index practically does not depend on r. The imaginary part of the index n increases when the central wire thickness r decreases, but this dependence is rather weak. Both $\mathrm{Re}\, n$ and $\mathrm{Im}\, n$ grow dramatically for $r \le l_s$ (l_s is shown by the dashed purple vertical line). This is due to the penetration of the THz field into the metal, i.e., it is a plasmonic effect.

The WKB solution for the radial field E_ρ in the cross section of this coax waveguide is shown for the last 3 mm of the propagation toward the tip in Figure 3.4(c). The following of the adiabatic change and the energy concentration are evident in this panel. The penetration into the metal of the tangential (to the metal surface) field components E_y and H_φ is noticeable in Figure 3.4(d)-(e). Note that the units of these field components are arbitrary but consistent between the panels. The intensity I of the THz field (relative to the intensity I_0 at the entrance of the waveguide) as a function of the waveguide outer radius $R = r + a$ is shown by the red line in Figure 3.4(f). Dramatically, it shows the adiabatic nanoconcentration and the intensity increase by more than two orders of magnitude for the initial waveguide radius $R = 300\,\mu\mathrm{m}$ toward $R = 300\,n\mathrm{m}$. However, the increase of the adiabatic parameter δ [plotted by the blue line in Figure 3.4(f)] for $R \le 1\,\mu\mathrm{m}$ shows that these results can only be trusted for $R \ge 1\,\mu\mathrm{m}$.

3.6.3 Advantages of Elongated Coaxial Cable

For the true 2d nanoconcentration of the THz radiation below this micron-scale radius, similar to the 1d case of the wedge, to preserve the adiabaticity, a funnel-like tapering is

necessary. Generally, the tapering of the central wire and that of the outer metal shell do not need to be the same. However, we found that better results are obtained when it is the case, i.e., when the waveguide is tapered-off self-similarly. In specific calculations, as everywhere in this thesis, we assume that the metal of the waveguide is silver, the dielectric is vacuum, and the frequency is 1 THz. Doing so, we have found the corresponding grading of the waveguide using Eq. (3.11) and setting $\delta = 0.05$, which is small enough to satisfy the adiabaticity very well. In this case, indeed, we have used the corresponding dispersion relation Eq. (3.27). The obtained shape of the waveguide is a strongly-elongated funnel, as shown in Figure 3.5(a)-(c). These figures display the THz fields that we have calculated in the WKB approximation for this waveguide. As one can see from these figures, within the last half micron of the propagation, the electric and magnetic fields of the THz wave efficiently follow the adiabatically curved waveguide. The penetration into the metal of the tangential (to the metal-dielectric interfaces) field components for $y < 400\,\mu$m is evident in Figure 3.5(b)-(c). The longitudinal electric field component E_y is significantly localized in the central metal wire [Figure 3.5 (b)], which is a plasmonic effect.

The dependence of the THz field intensity in the gap (relative to the intensity I_0 at the entrance of this funnel) on the total radius of the waveguide R is shown in Figure 3.5(d) by the red line. In this case, the adiabatic concentration is very efficient. The intensity of the THz radiation increases by a factor of $\times 5$ when it is compressed from the initial radius of $R = 1\,\mu$m to the radius $R \approx 250\,nm$. The penetration of the fields into the metal for smaller values of the radius R (tighter confinement) causes losses that dominate over the effect of the concentration.

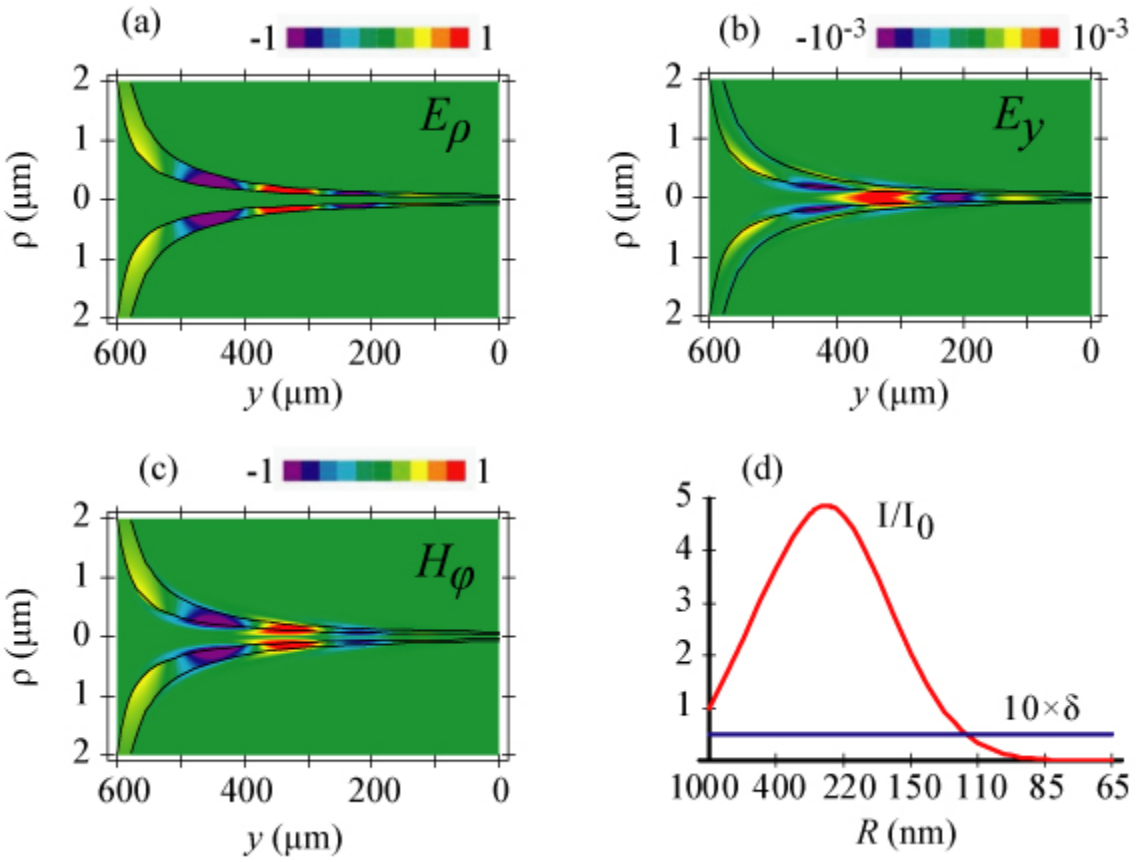

Figure 3.5. (color) Adiabatic terahertz energy concentration in a self-similarly curved, funnel-shaped coaxial waveguide, where the metal is silver, and the dielectric in the gap is vacuum. The dielectric gap is between the pair of the neighboring curved lines, and the metal is everywhere else. (a) Instantaneous distribution of the radial (transverse) component E_ρ of the electric field of the guided THz wave as a function of the propagation coordinate along the wedge y for the last $600\,\mu m$ of the propagation. (b) The same for the longitudinal electric field component E_y. (c) The same for transverse magnetic field H_φ, whose lines form circles around the central metal wire. The units of these field components are arbitrary but consistent between the panels. (d) The THz intensity I as a function of the waveguide radius R, displayed relative to the intensity I_0 at the beginning of the waveguide (red line). The adiabatic parameter δ multiplied by a factor of 10 as a function of R (blue line). The values of the radius R shown at the ticks correspond to those of y shown in panels (a)-(c).

Again, we remind the reader that this funnel waveguide is a continuation and termination for the straight cone that yields the field enhancement by $\times 50$ for $R = 1\,\mu\text{m}$ [see Figure 3.4(f)].

Consecutively, these two waveguides (the initial cone continued and terminated by the funnel) are very efficient, adiabatically compressing the THz radiation from the initial radius $R = 300\,\mu\text{m}$ to the radius $R = 250\,n\text{m}$ increasing its intensity by a factor $\times 250$. Even for the final radius $R = 100\,n\text{m}$, the total THz intensity is increased by a factor of $\times 10$ (which is the products of factors $\times 50$ for the cone part and $\times 0.2$ for the funnel. Thus, the optimally graded plasmonic-metal 2d waveguide is very efficient in the concentration and guidance of the THz fields with the transverse radius of confinement $R \propto 100\,n\text{m}$.

3.7 Concluding Remarks

To discuss these results, we have shown that the THz radiation can be concentrated to the $\sim 100\,n\text{m}$ transverse size in adiabatically graded plasmonic (metal/dielectric) waveguides. In the optimum adiabatically-graded, coaxial waveguide, which consists of the initial cone terminated with a funnel, the radiation of a 1 THz frequency whose wavelength is $300\,\mu\text{m}$ can be compressed to a spot of $250\,n\text{m}$ radius, where its intensity increases by a factor of $\times 250$. Even in the case of the extreme compression to a spot of the $100\,n\text{m}$ radius, the THz intensity is enhanced by one order of magnitude with respect to the initial intensity of the $300\,\mu\text{m}$ spot at the entrance of the waveguide. The physical process that limits the extent of this spatial concentration is the skin effect, i.e., penetration of the radiation into the metal that causes the

losses: the THz field penetrates the depth of $l_s = 30 - 60\,nm$ of the metal, which by the order of magnitude determines the ultimate localization radius.

The THz nanoconcentration predicted in this Chapter for optimally-graded adiabatic plasmonic waveguides provides unique opportunities for THz science and technology, of which we will mention below just a few. The nanoconcentration of the THz radiation will provide the THz ultramicroscopy with a THz source of unprecedented spatial resolution and brightness. The increase of the THz intensity by two orders of magnitude along with the novel high-power THz sources [96] would allow the observation of a wide range of electronic and vibrational nonlinear effects in metal, semiconductors, insulators, and molecules.

These nonlinear THz phenomena can be used to investigate the behavior of various materials in ultrastrong fields, for nonlinear spectroscopy (including multidimensional spectroscopy), and for monitoring and detection of various environmental, biological, and chemical objects and threats such as single bacterial spores and viruses. Such applications will certainly be helped by very large absorption cross sections of various materials in the THz region. A distinct and significant advantage of the adiabatic nanofocusing is that the THz energy is mostly concentrated in the hollow region of the waveguide, whose size can be made comparable with the size of the objects of interest: in the range from 1 micron to $70\,n\mathrm{m}$, which is a typical range for bacteria and their spores, and viruses. This will assure high sensitivity and low background for the objects that are confined inside these waveguides.

Consider as a specific example the spectroscopy or detection of single particles, such as, e.g., anthrax spores, in the air. A sample containing the suspected nanoparticles in a gas, which can be

air for the frequencies in the transparency windows, can be pumped through a THz waveguide, and the detection can be made for each particle in the gas separately on the basis of the two-dimensional nonlinear THz spectra that are expected to be highly informative for the detection and elimination of the false-positive alarms. Likewise, many other scientific, technological, environmental, and defense applications may become possible.

Chapter 4. Theory of Spoof Plasmons in Non-Perfect Conductors

4.1 Introduction to Spoof Plasmons

In the previous Chapter we have introduced a method that allows one to concentrate terahertz (THz) radiation on the nanoscale [95]. This method is the only one to date that allows for nanoconcentration of THz radiation. To accomplish such a nanoconcentration, a tapered wedge or coaxial cable should be used. The ultimate limit of nanoconcentration is set by the skin-depth of the metal. This shows that deviation of real metals from being perfect conductors is important even for THz frequencies. Theoretically, one can adabatically concentrate the THz field on the periodically corrugated surface of perfect conductor to an infinitely small spot using so-called spoof plasmons; however, we show here that for real metals it is not so. In this chapter, the possibility of focusing and guiding of THz spoof plasmons on the periodically corrugated interface between a non-perfect conductor and a dielectric is analyzed.

The appearance of the paper by Ebbesen et al. [105] reporting extraordinary optical transmission (EOT) through perforated metal films attracted great attention to the study of the optical properties of subwavelength apertures. It was found [105] that a metal film pierced with subwavelength holes transmits much more light than is expected according to the Bethe theory [106]. The transmission efficiency can exceed unity when normalized to the area of the holes.

Experiments have shown that this unusual optical property is due to the coupling of light to plasmons on the surface of the periodically corrugated metal film. Such a connection between EOT and plasmons was later proven theoretically in Ref. [107]. The enhanced transmission of THz radiation through a metal surface with subwavelength holes was also observed [108-110].

It is known that for most metals the plasma frequency ω_p is in the visible or near-infrared region of the spectrum due to the large free electron density [37]. Therefore, in the terahertz region surface plasmon polaritons do not propagate at the metal/dielectric interface. However, Pendry et al. [90] have shown that bound electromagnetic waves mimicking ("spoofing") surface plasmon polaritons can be sustained even by a perfect conductor surface, provided that it is periodically corrugated [90]. This result highlighted the possibility of creating "designer" ("spoof") SPP-like modes with an almost arbitrary dispersion generated through the structure rather than the material composition. The experimental demonstration of the designer plasmon surface modes supported by a two-dimensional hole array in the microwave regime was done in Ref. [111] using periodically arranged hollow brass tubes.

To date, theoretical considerations of such an interesting phenomenon as spoof plasmons have only been based on perfect metal descriptions [91, 112, 113]. The first attempt to propose focusing the spoof plasmons was done for a perfectly conducting corrugated wire [62]. As was already discussed, it is important to consider the deviation of a real metal from the ideal metal, especially since the most important characteristics of the focusing - the focus size and propagation length - are limited by this deviation. In this Chapter, we consider the influence of the finite skin depth on spoof plasmons. Specifically, we obtain the dispersion relation for the

spoof plasmons in case of non-perfect metal, we investigate their propagation length in real metals, and we also establish limits on the concentration of terahertz fields by means of spoof plasmons.

4.2 Theory of Planar Spoof Plasmons at a Perfect Conductor

The theory of the spoof plasmons on a periodic corrugation of the flat surface of a perfect conductor has been investigated in two papers [91, 114]. To derive the dispersion relation for such modes, consider a one-dimensional array of grooves of width a and depth h separated by a lattice constant d (see Figure 4.1).

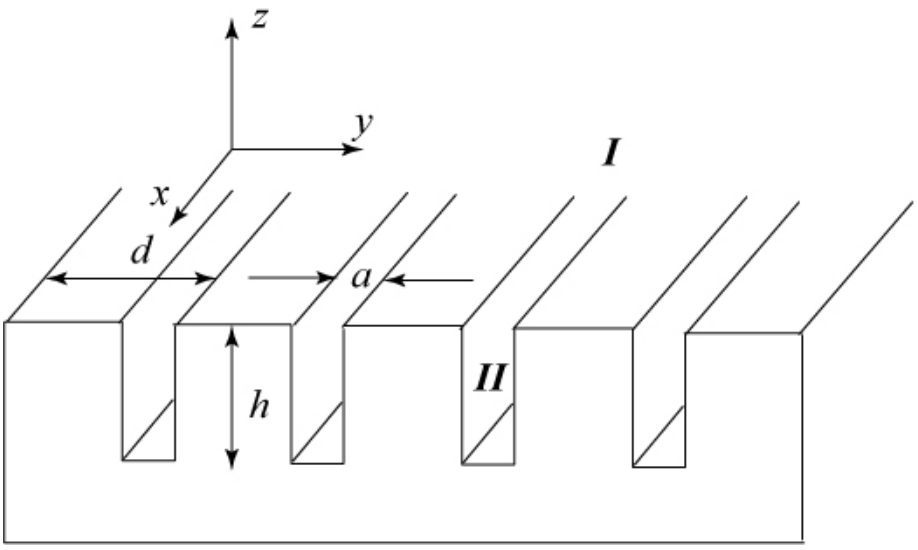

Figure 4.1. An array of grooves cut in a perfect metal of width a and depth h with period of the system d. The region I is a vacuum with $\varepsilon_d = 1$.

The calculation of reflectance coefficients will lead to the dispersion relation for the spoof plasmons in this system, because the surface mode resonance corresponds to a divergence in the

reflectivity. The total field in region I is the sum of the incident field and the reflected fields of order n. Therefore,

$$E_y^{\mathrm{I}} = \frac{1}{\sqrt{d}}\left(e^{ik_y y} e^{ik_z z} + \sum_{n=-\infty}^{\infty} \rho_n e^{ik_y^{(n)} y} e^{-ik_z^{(n)} z} \right), \tag{4.1}$$

$$H_x^{\mathrm{I}} = -\frac{1}{\sqrt{d}}\left(\frac{k_0}{k_z} e^{ik_y y} e^{ik_z z} - \sum_{n=-\infty}^{\infty} \rho_n \frac{k_0}{k_z^{(n)}} e^{ik_y^{(n)} y} e^{-ik_z^{(n)} z} \right)$$

where $k_0 = \omega / c$ is the wave vector in vacuum, $k_z^{(n)} = \sqrt{k_0^2 - \left(k_y^{(n)}\right)^2}$ with $k_y^{(n)} = k_y + 2\pi n / d$ and ρ_n is the reflection coefficient associated with the diffraction order n. Here the region I is vacuum with dielectric function equal to 1. The fields inside the grooves can be written as a sum of the forward and backward propagating TM-modes:

$$E_y^{\mathrm{II}} = \frac{1}{\sqrt{a}}\left(C^+ e^{-ik_0 z} - C^- e^{ik_0 z} \right), \tag{4.2}$$

$$H_x^{\mathrm{II}} = \frac{1}{\sqrt{a}}\left(C^+ e^{-ik_0 z} + C^- e^{ik_0 z} \right).$$

For this system the continuity of E_y and H_x should be satisfied at the boundary $z = 0$:

$$H_y^{\mathrm{I}}\Big|_{z=0} = H_y^{\mathrm{II}}\Big|_{z=0}, \qquad E_y^{\mathrm{I}}\Big|_{z=0} = E_y^{\mathrm{II}}\Big|_{z=0}. \tag{4.3}$$

Using Eqs. (4.1)-(4.3), one can obtain that

$$\frac{1}{\sqrt{d}}\left(e^{ik_y y} + \sum_{n=-\infty}^{\infty} \rho_n e^{ik_y^{(n)} y} \right) = \frac{C^+}{\sqrt{a}}\left(1 - e^{2ik_0 h} \right), \tag{4.4}$$

$$-\frac{1}{\sqrt{d}}\left(\frac{k_0}{k_z} e^{ik_y y} - \frac{1}{\sqrt{d}} \sum_{n=-\infty}^{\infty} \rho_n \frac{k_0}{k_z^{(n)}} e^{ik_y^{(n)} y} \right) = \frac{C^+}{\sqrt{a}}\left(1 + e^{2ik_0 h} \right)$$

where the equation $C^- = C^+ e^{2ik_0 h}$ is used which is due to the fact that the region II is a perfect conductor; thus, $E_y^{\mathrm{II}}\Big|_{z=-h} = 0$. By multiplying the first of equations (4.4) by $\exp[-ik_y^{(m)} y]$ and

integrating the right hand side over the unit cell and the left one over the groove locations we can obtain the following equation for the reflection coefficients

$$\rho_m = -\delta_{m0} + C^+\left(1 - e^{2ik_0h}\right)S_m\,, \tag{4.5}$$

where

$$S_m = \frac{1}{\sqrt{ad}}\int_{-a/2}^{a/2} e^{ik_y^{(m)}y}dy = \sqrt{\frac{a}{d}}\,\frac{\sin\left(k_y^{(m)}a/2\right)}{k_y^{(m)}a/2} \tag{4.6}$$

is the overlap integral between the n th-order plane wave and the fundamental TM mode. Then the second of equations (4.4) together with Eq. (4.5) and its integration over the groove locations gives

$$-\left(\frac{k_0}{k_z}S_0 + \sum_{n=-\infty}^{\infty}\delta_{n0}\,\frac{k_0}{k_z^{(n)}}S_n - \sum_{n=-\infty}^{\infty}C^+\left(1-e^{2ik_0h}\right)\frac{k_0}{k_z^{(n)}}S_n^2\right) = C^+\left(1+e^{2ik_0h}\right). \tag{4.7}$$

Therefore, the coefficient C^+ is

$$C^+ = -\frac{2\left(k_0/k_z\right)S_0}{\left(1+e^{2ik_0h}\right) - \left(1-e^{2ik_0h}\right)\sum_{n=-\infty}^{\infty}\left(k_0/k_z^{(n)}\right)S_n^2}\,. \tag{4.8}$$

Finally, substitution of this coefficient into Eq. (4.5) yields the expression for the reflection coefficients

$$\rho_n = -\delta_{n0} - \frac{2i\left(k_0/k_z\right)\tan\left(k_0h\right)S_0S_n}{1 - i\tan\left(k_0h\right)\sum_{n=-\infty}^{\infty}\left(k_0/k_z^{(n)}\right)S_n^2}\,, \tag{4.9}$$

If $\lambda_0 >> d$, only the specular reflection order, with coefficient ρ_0 needs to be taken into account and thus

$$\rho_0 = -\frac{1 + i\left(k_0/k_z\right)\tan\left(k_0h\right)S_0^2}{1 - i\left(k_0/k_z\right)\tan\left(k_0h\right)S_0^2}\,. \tag{4.10}$$

For the case $k_y > k_0$, i.e. $k_z = i\sqrt{k_y^2 - k_0^2}$, the dispersion relation is the pole of equation (4.10):

$$\frac{\sqrt{k_y^2 - k_0^2}}{k_0} = S_0^2 \tan(k_0 h), \tag{4.11}$$

Note that this is the dispersion relation of the surface electromagnetic modes which propagate on the 1D array of grooves in the perfect conductor. It is worth mentioning here that the same dispersion (4.11) can be obtained by substituting the array of grooves with a homogenous anisotropic dielectric of height h at the top of the perfect conductor. This layer is called an effective medium. The parameters for the effective medium in the case of an ideal metal are the following [91]:

$$\varepsilon_x = d/a, \quad \varepsilon_y = \varepsilon_z = \infty \tag{4.12}$$

$$\mu_x = 1, \quad \mu_y = \mu_z = a/d.$$

However, even for the THz part of the spectrum, real metals deviate from a perfect conductor [87]. If one wants to describe the concentration of spoof plasmons, losses should be taken into account. Later in this chapter, we consider the possibility of concentrating THz spoof plasmons in real metals. Periodic corrugation in real metals also can be described by the effective medium approximation as long as parameters of the system a and d are much smaller than the wavelength of the wave under consideration. Therefore, the next section is devoted to the theoretical description of the effective medium for a lossy metal periodically cut with planar grooves.

4.3 Effective Medium Approximation for Metal with Losses

For the purpose of describing grooves in our system, let us consider a regular assembly of thin parallel plates made of non-perfect metal with permittivity ε_m placed in a dielectric medium with permittivity ε_g and thickness a. Let the period of this system be d. Now suppose that a plane monochromatic wave is propagating through the array of such plates and assume first that the electric vector of the monochromatic wave is perpendicular to the metal plates. When a and d are much smaller than the wavelength of light, the field in the medium and in the metal may be considered as uniform. At the same time, the normal component of the electric displacement must be continuous across the surface. Therefore the vector $\mathbf{D}$ should have the same value inside the metal or in the medium. If $\mathbf{E}_1$ and $\mathbf{E}_2$ are the electric fields in a metal and the dielectric medium, correspondingly; then,

$$\mathbf{E}_1 = \frac{\mathbf{D}}{\varepsilon_m}, \quad \mathbf{E}_2 = \frac{\mathbf{D}}{\varepsilon_g}. \tag{4.13}$$

The mean field $\mathbf{E}$ averaged over the total volume is

$$\mathbf{E} = \frac{\frac{(d-a)\mathbf{D}}{\varepsilon_m} + \frac{a\mathbf{D}}{\varepsilon_g}}{d}, \tag{4.14}$$

The effective dielectric constant ε_y, combined with assumption that $|\varepsilon_m| >> \varepsilon_g$ (valid for the terahertz region), is the following

$$\varepsilon_y = \frac{\mathbf{D}}{\mathbf{E}} = \frac{d}{\frac{(d-a)}{\varepsilon_m} + \frac{a}{\varepsilon_g}} \approx \frac{d}{a}\varepsilon_g, \tag{4.15}$$

Next let us suppose that the electric vector of the incident field is parallel to the plates. Therefore, the electric field $\mathbf{E}$ must be continuous across the surface or, in other words, $\mathbf{E}$ has the same value inside the metal and in the dielectric medium. The electric displacement in two regions is

$$\mathbf{D}_1 = \varepsilon_m \mathbf{E}\,, \quad \mathbf{D}_2 = \varepsilon_g \mathbf{E}\,. \tag{4.16}$$

which give the following mean electric displacement

$$\mathbf{D} = \frac{(d-a)\varepsilon_m + a\varepsilon_g}{d}\mathbf{E}\,. \tag{4.17}$$

Hence, the effective dielectric constants in this case are

$$\varepsilon_x = \varepsilon_z = \frac{\mathbf{D}}{\mathbf{E}} = \frac{(d-a)\varepsilon_m + a\varepsilon_g}{d} \approx (1-\frac{a}{d})\varepsilon_m\,. \tag{4.18}$$

The last part of the formula (4.18) was obtained using approximation $|\varepsilon_m| >> \varepsilon_g$.

In order to acquire the magnetic permeabilities of the considered effective medium, i.e. μ_x, μ_y and μ_z, one should consider the Maxwell equations (1.1)-(1.2).

For the TM mode, the only remaining components of the electric and magnetic fields are H_x, E_y and E_z, which satisfy the following equations

$$\frac{\partial H_x}{\partial z} = -ik_0\varepsilon_y E_y\,, \quad \frac{\partial H_x}{\partial y} = ik_0\varepsilon_z E_z\,, \tag{4.19}$$

$$\frac{\partial E_z}{\partial y} - \frac{\partial E_y}{\partial z} = ik_0\mu_x H_x\,,$$

where $k_0 = \omega/c$. After some straightforward algebra, the equation for μ_x takes the form

$$\frac{k^2}{\varepsilon_z} + \frac{k_g^2}{\varepsilon_y} = k_0^2\mu_x\,. \tag{4.20}$$

Here we applied the condition that $H_x \propto e^{i(ky+k_g z)}$, where k is the wave vector of the spoof plasmon along the propagation direction and k_g is the wave vector of the wave propagating along the plates (3.4):

$$k_g = k_0 \sqrt{\varepsilon_g} \left(1 + \frac{l_s (i+1)}{a} \right)^{1/2}. \tag{4.21}$$

Now, consider the TE mode. In this case the non-zero components are E_x, H_y and H_z The corresponding components of the Maxwell equations (1.1)-(1.2) are

$$\frac{\partial E_x}{\partial z} = -ik_0 \mu_y H_y, \quad \frac{\partial E_x}{\partial y} = ik_0 \mu_z H_z, \tag{4.22}$$

$$\frac{\partial H_z}{\partial y} - \frac{\partial H_y}{\partial z} = -ik_0 \varepsilon_x E_x.$$

This leads to the expression for μ_y

$$\frac{k^2}{\mu_z} + \frac{k_g^2}{\mu_y} = k_0^2 \varepsilon_x. \tag{4.23}$$

Note that due to symmetry $\mu_x = \mu_z$. Finally, combining equations (4.20) and (4.23) we derive the magnetic parameters for the effective medium

$$\mu_x = \mu_z = \frac{1}{k_0^2} \left(\frac{k^2}{\varepsilon_z} + \frac{k_g^2}{\varepsilon_y} \right), \tag{4.24}$$

$$\mu_y = \frac{k^2 \varepsilon_y + k_g^2 \varepsilon_z}{k_0^2 \varepsilon_x \varepsilon_z}.$$

where ε_x, ε_y and ε_z are given by the equations (4.15) and (4.18).

The effective medium approach permits the description of a non-perfect conductor periodically drilled with planar grooves. Therefore the region II, displayed in Figure 4.1 is a

non-perfect conductor that behaves as an homogeneous but anisotropic layer of thickness h with parameters (4.15), (4.18) and (4.24) on top of the perfect conductor (Figure 4.2).

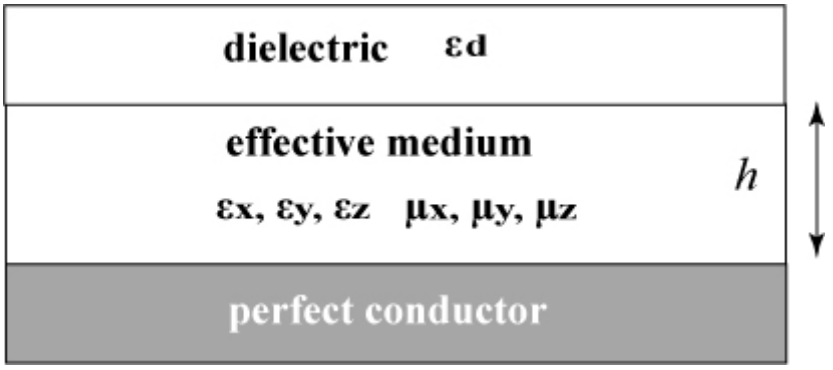

Figure 4.2. The structure with the grooves in the effective medium approximation. Parameters of effective medium are given by Eqs.(4.15), (4.18) and (4.24).

4.4 Theory of Spoof Terahertz Plasmons on Metals with Finite Conductivity

Using the effective medium approximation derived in Section 4.3, we can describe the TM-mode in the structure pictured in Figure 4.2. The magnetic and electric fields are

$$H_x = A\begin{cases} e^{-\kappa z}e^{iky}, z > 0 \\ \dfrac{\cos(k_g(z+h))}{\cos(k_g h)}e^{iky}, -\mathrm{h} < \mathrm{z} < 0 \end{cases}, \tag{4.25}$$

$$E_y = \frac{\partial_z H_x}{-ik_0\varepsilon_y} = A\begin{cases} -\dfrac{i\kappa}{k_0\varepsilon_d}e^{-\kappa z}e^{iky}, \ z > 0 \\ -\dfrac{ik_g}{k_0\varepsilon_y}\dfrac{\sin(k_g(z+h))}{\cos(k_g h)}e^{iky}, -\mathrm{h} < z < 0 \end{cases}, \tag{4.26}$$

$$E_z = \frac{\partial_y H_x}{ik_0\varepsilon_z} = \frac{Ak}{k_0}\begin{cases} \dfrac{1}{\varepsilon_d}e^{-\kappa z}e^{iky}, \ z > 0 \\ \dfrac{\cos(k_g(z+h))}{\varepsilon_z\cos(k_g h)}e^{iky}, -h < z < 0 \end{cases}. \tag{4.27}$$

where $\kappa = (k^2 - \varepsilon_d k_0^2)^{1/2}$, k is the spoof plasmon wave number and k_g is defined by Eq. (4.21). Note that the region $-h < z < 0$ is the effective medium; thus, ε_y and ε_z are given by the Eqs (4.15) and (4.18), correspondingly.

The magnetic fields are already matched at $z = 0$. The longitudinal electric field should also be continuous at $z = 0$. Therefore, the equation for κ is

$$\kappa = \frac{a\varepsilon_d}{d\varepsilon_g} k_g \tan(k_g h) . \tag{4.28}$$

This expression is obtained using the fact that $|\varepsilon_m| >> \varepsilon_g$, which is an extremely good approximation for the terahertz region since $|\varepsilon_m| \sim 10^6$ and the dielectric function in the grooves is $\varepsilon_g = 1$.

Eventually, we have the spoof plasmon wave number:

$$k = \sqrt{\varepsilon_d k_0^2 + \kappa^2} = \left(\varepsilon_d k_0^2 + \left(\frac{a\varepsilon_d}{d\varepsilon_g} \right)^2 k_g^2 \tan^2(k_g h) \right)^{1/2} \tag{4.29}$$

with k_g given by relation (4.21).

This is the dispersion relation for the spoof plasmons supported by the non-perfect metal with grooves in it. Formula (4.29) takes into account the finite conductivity of the metal by introducing the skin depth l_s (Eq. (3.1)), which is in the range from 30-120 nm for the terahertz part of the spectrum and equal to ~ 60 nm at a frequency of 1 THz for silver [87]. To illustrate the behavior of the spoof plasmons, we plot the real and imaginary part of the wave vector k as a function of the frequency $f = \omega / 2\pi$ in Figure 4.3(a).

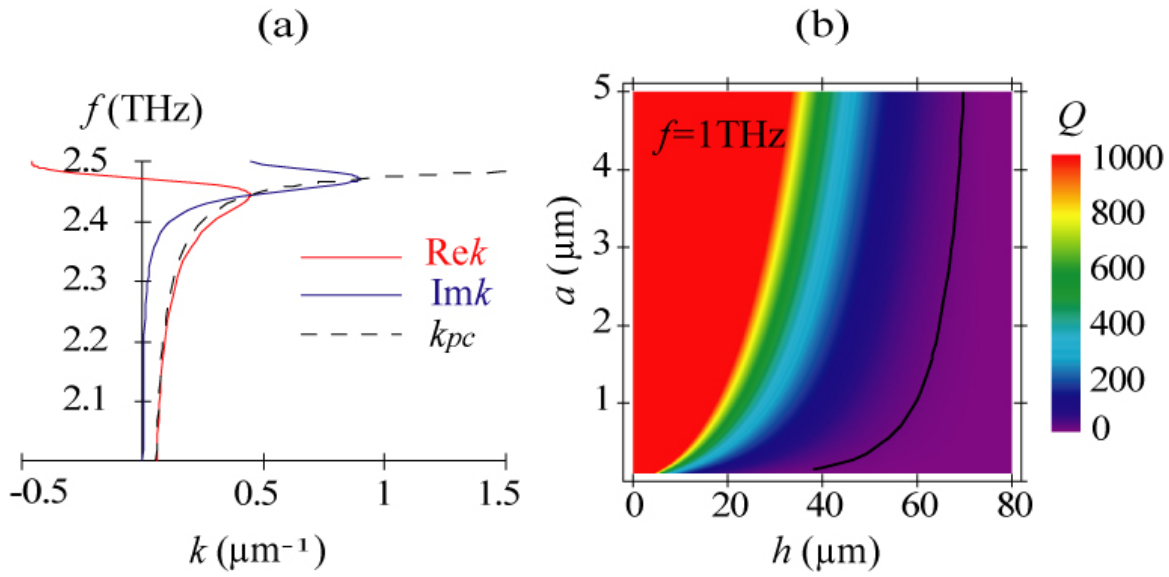

Figure 4.3. (color) (a) The dispersion relation of the spoof plasmons (frequency f versus wave vector k) supported by a 1D array of grooves with geometrical parameters $a/d = 0.3$, $a = 3\mu\text{m}$, $h = 30\mu\text{m}$. $\text{Re}\,k$ is denoted by the red line and $\text{Im}\,k$ by the blue line, while the black dashed line is the dispersion relation for a of perfect conductor. The dielectric functions ε_d and ε_g are chosen to be 1. (b) The spoof plasmons figure of merit Q as the function of a and h for $f = 1\ THz$ ($a/d = 0.3$). The black curve corresponds to $Q = 10$.

The dashed black line in Figure 4.3(a) corresponds to the dispersion of spoof plasmons on perfect metal. It can be seen that at resonant frequency, which is for given parameters $f \cong 2.5\,THz$, the wave vector k_{pc} is infinitely large. However, if losses are taken into account, $\text{Re}\,k$ has the maximum finite value (red curve) and a peak of $\text{Im}\,k$ appears (blue curve) near the resonance. The dispersion curve exhibits strong back bending and $\text{Re}\,k$ reaches negative values, such that $\text{Re}\,k \cdot \text{Im}\,k < 0$, which means that phase and energy propagate in different directions; an effect called negative refraction [4, 115].

Figure 4.3(b) depicts the quality factor $Q = \text{Re}\,k / \text{Im}\,k$ as a function of the geometrical parameters of the system, a and h at $f = 1\ THz$. Physically, Q shows how many oscillations a spoof plasmon undergoes before it dissipates due to the losses.

The figure of merit Q should be $>>1$ in order for spoof plasmons to be a well-defined excitation. The black curve in this figure shows when $Q=10$, so area to the left of the curve is suitable for propagation of THz field with spoof plasmons.

Besides Q, the other important propagation characteristics of spoof plasmons are the energy attenuation length (propagation length) $l_p = 1/(\mathrm{Im}\, k)$ and energy confinement in the dielectric $\xi = 1/(\mathrm{Re}\,\kappa)$. It is desired to have larger propagation lengths and good energy confinement. In Figure 4.4, these two parameters are shown as a function of the depth of the grooves, h. Note that the better the confinement is, the lower is the propagation length. Therefore, the optimum h is a compromise between these two parameters and it is different depending on whether longer propagation or better confinement is required. Spoof plasmons are extremely good for the propagation of THz fields: for example, for $h = 30\,\mu\mathrm{m}$, $f = 1\,THz$ and silver/air interface $l_p \cong 20\,\mathrm{mm}$ with $\xi \cong 100\,\mu\mathrm{m}$.

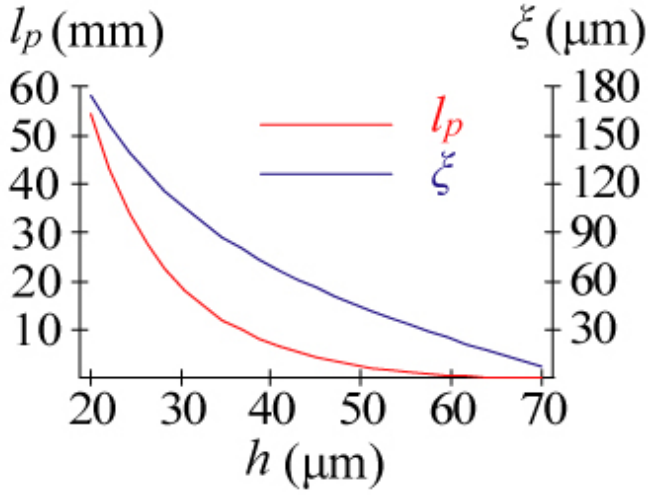

Figure 4.4. (color) The propagation length l_p (red curve) and confinement length ξ (blue curve) as functions of the depth of the grooves h at $f = 1\,THz$ for the parameters $a/d = 0.3$, $a = 3\,\mu\mathrm{m}$. Note the different scales on the right and left axes.

4.5 Adiabatic Concentration on Spoof Plasmon Structure

For some time spoof plasmons were considered as a promising tool for the concentration of THz radiation [62]. However, this assumption was based on the perfect conductor description which does not take losses into account. Here we will consider the possibility of focusing using the non-perfect metal with periodically drilled grooves and show that the concentration is limited at tens of micrometers.

In order to have small wavelength (good focusing) and high intensity, the wave vector of the spoof plasmon k given by Eq. (4.29) should be large. As one can see, k reaches a maximum when the argument under the tangent $k_g h \to \frac{\pi}{2}$. To estimate the position of the maximum we can say that $k_g \sim k_0$ and thus at the resonance, $h \to \frac{\lambda}{4}$. For the frequency 1 THz - $\lambda = 300 \mu m$, the resonant depth of the groove is around $75 \mu m$. The difference between k_g and k_0 determines the physical shape of the resonance. The dependence of real and imaginary parts of k as functions of h is shown in Figure 4.5, which confirms the resonant behavior of k and the estimate of the resonant position.

Therefore, in order to concentrate spoof plasmons one should adiabatically increase the depth of the groove until the wave vector k reaches the maximum or, in other words, adiabatically increase the thickness of the effective medium. With the intention of making the adiabatic concentration using spoof plasmons, one should keep the parameter of adiabaticity $\delta = \left| d(\mathrm{Re}\, k^{-1}) / dy \right|$ small compared to unity. For our computation we kept this parameter small,

equal to 0.1, which allows the determination of the dependence $h(y)$, i.e. the shape of the effective medium.

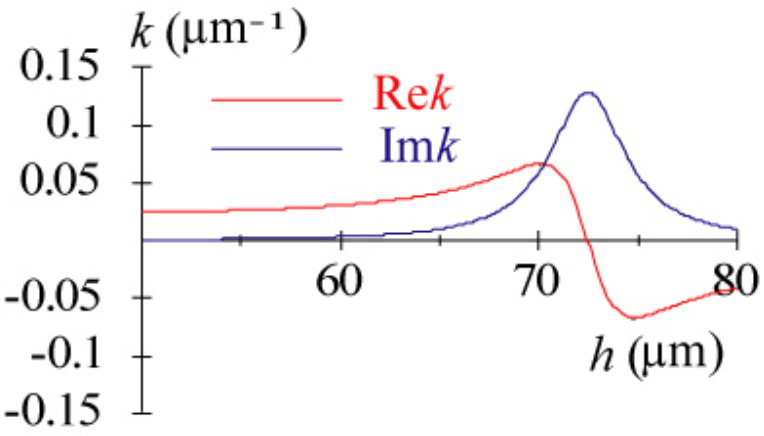

Figure 4.5. (color) The spoof plasmons wavevector k (Eq. (4.29)) as the function of the depth of the grooves h at $f = 1THz$ with the parameters $a/d = 0.3$, $a = 1\mu$m. The red and blue curves show $\mathrm{Re}\,k$ and $\mathrm{Im}\,k$, correspondingly.

Following the recipe given in Chapter 3, we have found the phase (eikonal) and amplitude of the adiabatic wave. The eikonal $\Phi(y)$ is given by the equation (3.7), where k is now defined by Eq. (4.29). Due to the conservation of the energy flux, $J(y)$ (Eq. (3.8)), the amplitude is $A = \sqrt{J(0)/J(y)}$.

The fields (4.25)-(4.27) multiplied by the eikonal exponent $e^{i\Phi(y)}$ and the amplitude A are plotted in plane yz in Figure 4.6(a)-(c) and the electric field intensity, I is in Figure 4.6(d). As one can see from this figure, when the depth of the grooves h is adiabatically increased (shown by the dashed black line), the spoof plasmons fields increases in intensity by a factor of $\times 1500$, while the wavelength decreases from $300\,\mu m$ to $40\,\mu m$, so the energy is concentrated.

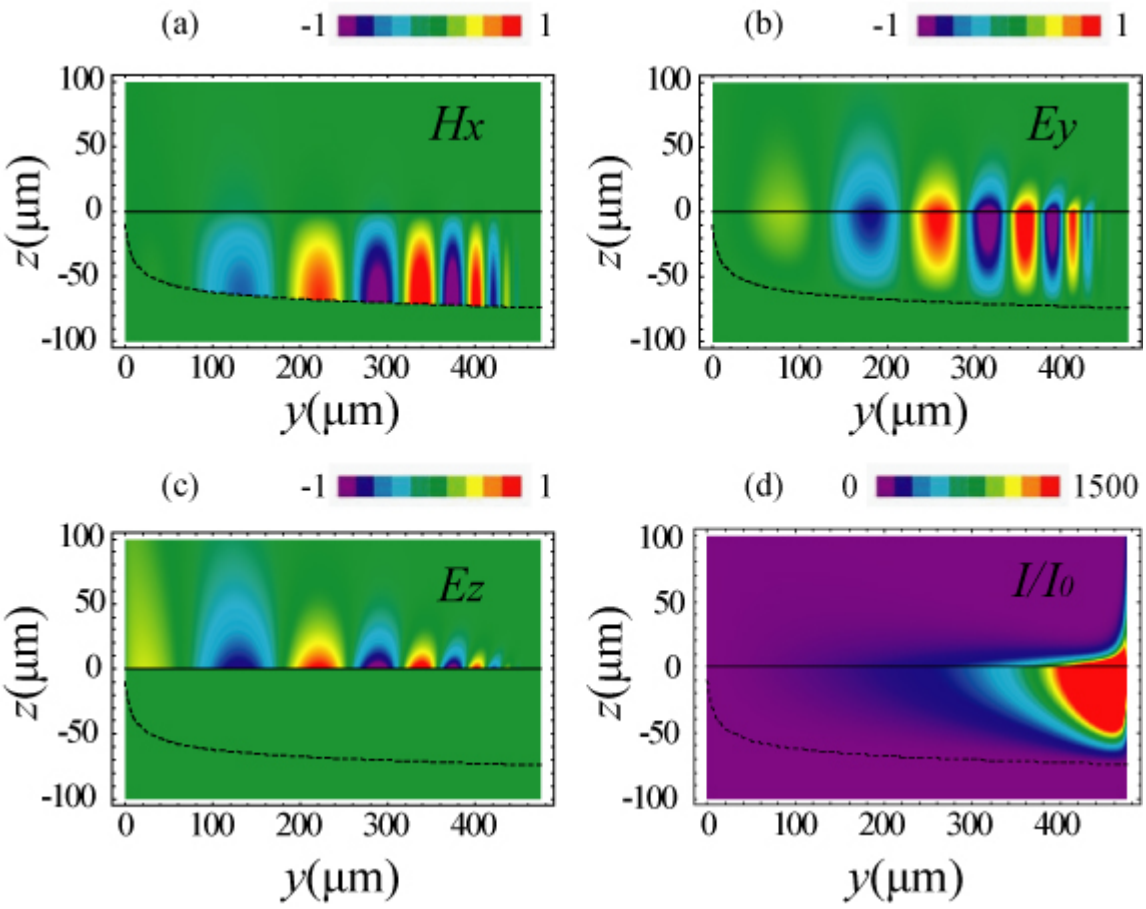

Figure 4.6. (color) Terahertz spoof energy concentration due to adiabatical increase of the thickness of the effective medium. (a) Instantaneous distribution of transverse magnetic field H_x as the function of the coordinate y along the propagation direction. (b) The same as in panel (a) but for the longitudinal electric field E_y. (c) The same as in panel (a) but for the transverse electric field E_z. The units of the fields are arbitrary but consistent between the panels. (d) The intensity of the spoof fields I, relative to the intensity I_0 at the point (0,0) in yz plane, as a function of y. The dashed black line represents the shape of the effective medium, i.e. $h(y)$.

The question now is how efficient is such a structure for the concentration; i.e., what is the minimum size of the hot spot. In the case of a perfect metal the size of the spot is not limited and can theoretically be infinitely small. However, we have considered a non-perfect conductor with

the losses introduced through the skin depth l_s (Eq. (3.1)). In order to have a strong resonance and high k, the parameter l_s / a or l_s / d should be small. Since for a given frequency the skin depth l_s is fixed, one has to increase the size of the system. On the other hand, the increase of d leads to diffraction when d becomes comparable with wavelength λ_{spoof}. To analyze this diffraction limitation we need to find the largest value of $k(d)$ (Eq. (4.29)) at which $2\pi / k_{\max}(d) >> d$ still holds. In other words, how sharp the resonance (Figure 4.5) can be without causing diffraction at $k_{\max}$.

In Figure 4.7, $\lambda_{\min}$ describes the minimum size of the spot at the resonant depth of grooves $h_{\max}$ as the function of the size of the system d. In order to avoid diffraction, the size of the spot $\lambda_{\min}$ should be much larger then d (blue line). The condition $\lambda_{\min} \approx 3d$ (intersection of red ad dashed black lines) gives the size of the hot spot of $\sim 40\,\mu m$, which coincides with Figure 4.6. So the wavelength that is concentrated by means of planar spoof plasmons cannot be smaller than $30-40\,\mu m$, i.e., it is on the microscale.

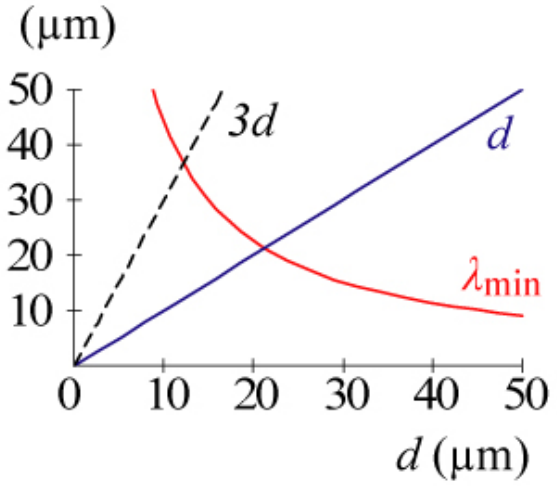

Figure 4.7. (color) Estimate of the size of the spot for concentration by means of spoof plasmons. The red curve shows the dependence $\lambda_{\min}(d) = 2\pi / k_{\max}(d)$. The frequency is $f = 1\,THz$ with $a / d = 0.3$.

4.6 Conclusions

To briefly conclude, spoof plasmons are a very interesting and promising phenomenon, which has been recently proposed [90]. They can be used for guiding and focusing of THz radiation at the interface of corrugated metal. In this Chapter we have developed the theory that describes the designer plasmons in the case of a non-perfect conductor, i.e., in the system with losses. The derived dispersion relation allowed us to investigate the propagation characteristics, such as length of propagation l_p, energy confinement length ξ and quality factor Q, as functions of the geometrical parameters of the system, a, d and h. Even with dissipation of energy, by selecting optimum parameters of the structure, one can provide good guidance and confinement of THz field with spoof plasmons. We have also considered the possibility of focusing THz fields by spoof plasmons. By deepening the grooves, one can reach focusing of spoof plasmons to a spot with the size of $30-40\,\mu m$. This is three orders of magnitude worse than concentration of THz radiation proposed in Chapter 3, but it is achieved on a planar structure, convenient for applications. Also it can be used as a starting approach for consequent concentration using coax or tapered parallel metal plates.

References

1. Landau, L.D. and E.M. Lifshitz, *Theoretical Physics. The Classical Theory of Fields*. Vol. 2. 1988, Moscow: Nauka.

2. Born, M. and E. Wolf, *Principles of Optics*. 1999, Cambridge: Cambridge University Press.

3. Pendry, J.B., *Negative refraction makes a perfect lens.* Physical Review Letters, 2000. **85**(18): p. 3966.

4. Veselago, V.G., *Electrodynamics of substances with simultaneously negative values of sigma and mu.* Soviet Physics Uspekhi, 1968. **10**(4): p. 509-514.

5. Shvets, G., *Photonic approach to making a material with a negative index of refraction.* Physical Review B, 2003. **67**(3): p. 35109.

6. Houck, A.A., J.B. Brock, and I.L. Chuang, *Experimental observations of a left-handed material that obeys Snell's law.* Physical Review Letters, 2003. **90**(13): p. 137401.

7. Smith, D.R. and N. Kroll, *Negative refractive index in left-handed materials.* Physical Review Letters, 2000. **85**(14): p. 2933-2936.

8. Luo, C.Y., et al., *Negative refraction without negative index in metallic photonic crystals.* Optics Express, 2003. **11**(7): p. 746-754.

9. Fang, N., et al., *Sub-diffraction-limited optical imaging with a silver superlens.* Science, 2005. **308**(5721): p. 534-537.

10. Melville, D. and R. Blaikie, *Super-resolution imaging through a planar silver layer.* Opt. Express, 2005. **13**(6): p. 2127-2134.

11. Liu, Z., et al., *Rapid growth of evanescent wave by a silver superlens.* Applied Physics Letters, 2003. **83**(25): p. 5184-5186.

12. Larkin, I.A. and M.I. Stockman, *Imperfect perfect lens.* Nano Lett., 2005. **5**(2): p. 339-343.

13. Johnson, P.B. and R.W. Christy, *Optical-constants of noble-metals.* Physical Review B, 1972. **6**(12): p. 4370-4379.

14. Stockman, M.I., *Criterion for negative refraction with low optical losses from a fundamental principle of causality.* Physical Review Letters, 2007. **98**(17): p. 177404-4.

15. Wood, R.W., *On a remarkable case of uneven distribution of light in a diffraction grating spectrum.* Proceedings of the Physical Society of London, 1902. **18**(1): p. 269-275.

16. Garnett, J.C.M., *Colours in metal glasses, in metallic films, and in metallic solutions. II.* Philosophical Transactions of the Royal Society of London. Series A, Containing Papers of a Mathematical or Physical Character, 1906. **205**: p. 237-288.

17. Mie, G., *Contributions to the optics of turbid media, particularly of colloidal metal solutions.* Ann. Phys, 1908. **25**(3): p. 337-445.

18. Bohm, D. and D. Pines, *A collective description of electron interactions: III. Coulomb interactions in a degenerate electron gas.* Physical Review, 1953. **92**(3): p. 609.

19. Mott-Smith, H.M. and I. Langmuir, *The theory of collectors in gaseous discharges.* Physical Review, 1926. **28**(4): p. 727.

20. Tonks, L. and I. Langmuir, *Oscillations in ionized gases.* Physical Review, 1929. **33**(2): p. 195.

21. Pines, D., *Collective energy losses in solids.* Reviews of Modern Physics, 1956. **28**(3): p. 184.

22. Fano, U., *Atomic theory of electromagnetic interactions in dense materials.* Physical Review, 1956. **103**(5): p. 1202.

23. Ritchie, R.H., et al., *Surface-plasmon resonance effect in grating diffraction.* Physical Review Letters, 1968. **21**(22): p. 1530.

24. Otto, A., *Excitation of nonradiative surface plasma waves in silver by the method of frustrated total reflection.* Zeitschrift für Physik A Hadrons and Nuclei, 1968. **216**(4): p. 398-410.

25. Kretschmann, E. and H. Raether, *Radiative decay of nonradiative surface plasmons excited by light* Zeitschrift fuer Naturforschung, Teil A: Astrophysik, Physik und Physikalische Chemie, 1968. **23**(12): p. 2135-6.

26. Fleischmann, M., P.J. Hendra, and A.J. McQuillan, *Raman spectra of pyridine adsorbed at a silver electrode.* Chemical Physics Letters, 1974. **26**(2): p. 163-166.

27. Jeanmaire, D.L. and R.P. Van Duyne, *Surface Raman spectroelectrochemistry: Part I. Heterocyclic, aromatic, and aliphatic amines adsorbed on the anodized silver electrode.* Journal of Electroanalytical Chemistry, 1977. **84**(1): p. 1-20.

28. Kneipp, K., et al., *Single molecule detection using surface-enhanced Raman scattering (SERS).* Physical Review Letters, 1997. **78**(9): p. 1667.

29. Nie, S. and S.R. Emory, *Probing single molecules and single nanoparticles by surface-enhanced Raman scattering.* Science, 1997. **275**(5303): p. 1102-1106.

30. Lewis, A., et al., *Scanning optical spectral microscopy with 500Å spatial resolution.* Biophys. J., 1983. **41**: p. 405a.

31. Pohl, D.W., W. Denk, and M. Lanz, *Optical stethoscopy: Image recording with resolution lambda/20.* Applied Physics Letters, 1984. **44**(7): p. 651-653.

32. Novotny, L. and B. Hecht, *Principles of Nano-optics*. 2006, Cambridge, New York: Cambridge University Press.

33. Bergman, D.J. and M.I. Stockman, *Surface plasmon amplification by stimulated emission of radiation: Quantum generation of coherent surface plasmons in nanosystems.* Physical Review Letters, 2003. **90**(2): p. 027402-1-4.

34. Noginov, M.A., et al., *Demonstration of a spaser-based nanolaser.* Nature, 2009. **460**(7259): p. 1110-1112.

35. Jackson, J., *Classical Electrodynamics*. 1998: Wiley.

36. Stratton, J.A., *Electromagnetic Theory*. 1941, New York and London: McGraw-Hill Book Company.

37. Ashcroft, N.W. and N.D. Mermin, *Solid State Physics*. 1976, Philadelphia: Saunders College.

38. Sommerfeld, A., *Ueber die fortpflanzung elektrodynamischer wellen längs eines drahtes.* Ann. Phys. Chem., 1899. **67**: p. 233 - 290.

39. Zenneck, J., *Fortplfanzung ebener elektromagnetischer Wellen längs einer ebenen Leiterfläche.* Ann. Phys., 1907. **23**: p. 846–866

40. Stockman, M.I., *Nanofocusing of optical energy in tapered plasmonic waveguides.* Physical Review Letters, 2004. **93**(13): p. 137404.

41. Landau, L.D. and E.M. Lifshitz, *Electrodynamics of continuous media*. 2 ed. Course of theoretical physics, ed. E.M. Lifshitz and L.P. Pitaevskii. Vol. 8. 1984, Oxford and New York: Pergamon. 460.

42. Gramotnev, D.K., *Adiabatic nanofocusing of plasmons by sharp metallic grooves: Geometrical optics approach.* Journal of Applied Physics, 2005. **98**(10): p. 104302 -1-11.

43. Durach, M., A. Rusina, and M.I. Stockman, *Toward full spatiotemporal control on the nanoscale.* Nano Letters, 2007. **7**(10): p. 3145-3149.

44. Verhagen, E., A. Polman, and L. Kuipers, *Nanofocusing in laterally tapered plasmonic waveguides.* Opt. Express, 2008. **16**(1): p. 45-57.

45. Ropers, C., et al., *Grating-coupling of surface plasmons onto metallic tips: a nanoconfined light source.* Nano Lett., 2007. **7**(9): p. 2784-2788.

46. Rabitz, H., et al., *Chemistry - whither the future of controlling quantum phenomena?* Science, 2000. **288**(5467): p. 824-828.

47. Apolonski, A., et al., *Observation of light-phase-sensitive photoemission from a metal.* Physical Review Letters, 2004. **92**(7): p. 073902-1-4.

48. Zeidler, D., et al., *Controlling attosecond double ionization dynamics via molecular alignment.* Physical Review Letters, 2005. **95**(20): p. 203003.

49. Shapiro, M. and P. Brumer, *Quantum control of bound and continuum state dynamics.* Physics Reports, 2006. **425**(4): p. 195-264.

50. Stockman, M.I., S.V. Faleev, and D.J. Bergman, *Coherent control of femtosecond energy localization in nanosystems.* Physical Review Letters, 2002. **88**(6): p. 67402-1-4.

51. Stockman, M.I. and P. Hewageegana, *Nanolocalized nonlinear electron photoemission under coherent control.* Nano Letters, 2005. **5**(11): p. 2325-2329.

52. Kubo, A., et al., *Femtosecond imaging of surface plasmon dynamics in a nanostructured silver film.* Nano Letters, 2005. **5**(6): p. 1123-1127.

53. Sukharev, M. and T. Seideman, *Phase and polarization control as a route to plasmonic nanodevices.* Nano Letters, 2006. **6**(4): p. 715-719.

54. Kubo, A., N. Pontius, and H. Petek, *Femtosecond microscopy of surface plasmon polariton wave packet evolution at the silver/vacuum interface.* Nano Lett., 2007. **7**(2): p. 470-475.

55. Sukharev, M. and T. Seideman, *Coherent control of light propagation via nanoparticle arrays.* Journal of Physics B: Atomic, Molecular and Optical Physics, 2007. **40**(11): p. S283-S298.

56. Aeschlimann, M., et al., *Adaptive subwavelength control of nano-optical fields.* Nature, 2007. **446**(7133): p. 301-304.

57. Wefers, M.M. and K.A. Nelson, *Programmable phase and amplitude femtosecond pulse shaping.* Optics Letters, 1993. **18**(23): p. 2032-2034.

58. Feurer, T., J.C. Vaughan, and K.A. Nelson, *Spatiotemporal coherent control of lattice vibrational waves.* Science, 2003. **299**(5605): p. 374-377.

59. Nomura, W., M. Ohtsu, and T. Yatsui, *Nanodot coupler with a surface plasmon polariton condenser for optical far/near-field conversion.* Applied Physics Letters, 2005. **86**(18).

60. Yin, L.L., et al., *Subwavelength focusing and guiding of surface plasmons.* Nano Letters, 2005. **5**(7): p. 1399-1402.

61. Verhagen, E., L. Kuipers, and A. Polman, *Enhanced nonlinear optical effects with a tapered plasmonic waveguide.* Nano Letters, 2007. **7**(2): p. 334-337.

62. Maier, S.A., et al., *Terahertz surface plasmon-polariton propagation and focusing on periodically corrugated metal wires.* Physical Review Letters, 2006. **97**(17): p. 176805.

63. Mailloux, R.J., *Phased Array Antenna Handbook*. 2005, Boston: Artech House Inc.

64. Lerosey, G., et al., *Time reversal of electromagnetic waves.* Physical Review Letters, 2004. **92**(19): p. 193904.

65. Lerosey, G., et al., *Time reversal of wideband microwaves.* Applied Physics Letters, 2006. **88**(15): p. 154101-3.

66. Lerosey, G., et al., *Focusing beyond the diffraction limit with far-field time reversal.* Science, 2007. **315**(5815): p. 1120-1122.

67. Ganichev, S. and W. Prettl, *Intense Terahertz Excitation of Semiconductors*. 2006: Oxford University Press.

68. Kaindl, R.A., et al., *Far-infrared optical conductivity gap in superconducting MgB2 Films.* Physical Review Letters, 2001. **88**(2): p. 027003.

69. Mickan, S.P., et al., *Label-free bioaffinity detection using terahertz technology.* Physics in Medicine and Biology, 2002. **47**(21): p. 3789-3795.

70. Mittleman, D.M., et al., *T-ray tomography.* Opt. Lett., 1997. **22**(12): p. 904-906.

71. Grosse, E., *THz radiation from free electron lasers and its potential for cell and tissue studies.* Physics in Medicine and Biology, 2002. **47**(21): p. 3755-3760.

72. Federici, J.F., et al., *THz imaging and sensing for security applications - explosives, weapons and drugs.* Semiconductor Science and Technology, 2005. **20**(7): p. S266-S280.

73. Smith, P.R., D.H. Auston, and M.C. Nuss, *Subpicosecond photoconducting dipole antennas.* Quantum Electronics, IEEE Journal of, 1988. **24**(2): p. 255-260.

74. Hu, B.B., et al., *Free-space radiation from electro-optic crystals.* Applied Physics Letters, 1990. **56**(6): p. 506-508.

75. Sun, F.G., G.A. Wagoner, and X.C. Zhang, *Measurement of free-space terahertz pulses via long-lifetime photoconductors.* Applied Physics Letters, 1995. **67**(12): p. 1656-1658.

76. Wu, Q. and X.C. Zhang, *Free-space electro-optic sampling of terahertz beams.* Applied Physics Letters, 1995. **67**(24): p. 3523-3525.

77. Auston, D.H. and K.P. Cheung, *Coherent time-domain far-infrared spectroscopy.* J. Opt. Soc. Am. B, 1985. **2**(4): p. 606-612.

78. Han, P.Y., et al., *A direct comparison between terahertz time-domain spectroscopy and far-infrared Fourier transform spectroscopy.* Journal of Applied Physics, 2001. **89**(4): p. 2357-2359.

79. Novotny, L. and S.J. Stranick, *Near-field optical microscopy and spectroscopy with pointed probes.* Annual Review of Physical Chemistry, 2006. **57**(1): p. 303-331.

80. Lewis, A., et al., *Near-field optics: from subwavelength illumination to nanometric shadowing.* Nat Biotech, 2003. **21**(11): p. 1378-1386.

81. Seelig, J., et al., *Nanoparticle-induced fluorescence lifetime modification as nanoscopic ruler: demonstration at the single molecule level.* Nano Letters, 2007. **7**(3): p. 685-689.

82. De Angelis, F., et al., *A hybrid plasmonic-photonic nanodevice for label-free detection of a few molecules.* Nano Letters, 2008. **8**(8): p. 2321-2327.

83. Chan, W.L., J. Deibel, and D.M. Mittleman, *Imaging with terahertz radiation.* Reports on Progress in Physics, 2007. **70**(8): p. 1325-1379.

84. Chen, H.-T., R. Kersting, and G.C. Cho, *Terahertz imaging with nanometer resolution.* Applied Physics Letters, 2003. **83**(15): p. 3009-3011.

85. Klein, N., et al., *A metal-dielectric antenna for terahertz near-field imaging.* Journal of Applied Physics, 2005. **98**(1): p. 014910-5.

86. Lecaque, R., S. Grésillon, and C. Boccara, *THz emission microscopy with sub-wavelength broadband source.* Opt. Express, 2008. **16**(7): p. 4731-4738.

87. Ordal, M.A., et al., *Optical properties of the metals Al, Co, Cu, Au, Fe, Pb, Ni, Pd, Pt, Ag, Ti, and W in the infrared and far infrared.* Applied Optics, 1983. **22**(7): p. 1099-1119.

88. Saxler, J., et al., *Time-domain measurements of surface plasmon polaritons in the terahertz frequency range.* Physical Review B, 2004. **69**(15): p. 155427.

89. Mills, D.L. and A.A. Maradudin, *Surface corrugation and surface-polariton binding in the infrared frequency range.* Physical Review B, 1989. **39**(3): p. 1569.

90. Pendry, J.B., L. Martin-Moreno, and F.J. Garcia-Vidal, *Mimicking surface plasmons with structured surfaces.* Science, 2004. **305**(5685): p. 847-848.

91. Garcia-Vidal, F.J., et al., *Surfaces with holes in them: new plasmonic metamaterials.* Journal of Optics A: Pure and Applied Optics, 2005(2): p. S97.

92. Keilmann, F., et al., *Extreme sub-wavelength resolution with a scanning radio-frequency transmission microscope.* Optics Communications, 1996. **129**(1-2): p. 15-18.

93. Keilmann, F., *FIR microscopy.* Infrared Physics & Technology, 1995. **36**(1): p. 217-224.

94. Kramer, A., et al., *The coaxial tip as a nano-antenna for scanning near-field microwave transmission microscopy.* Micron, 1996. **27**(6): p. 413-417.

95. Rusina, A., et al., *Nanoconcentration of terahertz radiation in plasmonic waveguides.* Optics Express, 2008. **16**(23): p. 18576-18589.

96. Hebling, J., et al., *High-power THz generation, THz nonlinear optics, and THz nonlinear spectroscopy.* Selected Topics in Quantum Electronics, IEEE Journal of, 2008. **14**(2): p. 345-353.

97. Shen, Y., et al., *Nonlinear cross-phase modulation with intense single-cycle terahertz pulses.* Physical Review Letters, 2007. **99**(4): p. 043901-4.

98. Komiyama, S., et al., *A single-photon detector in the far-infrared range.* Nature, 2000. **403**(6768): p. 405-407.

99. Ferguson, B. and X.-C. Zhang, *Materials for terahertz science and technology.* Nat Mater, 2002. **1**(1): p. 26-33.

100. Tonouchi, M., *Cutting-edge terahertz technology.* Nat Photon, 2007. **1**(2): p. 97-105.

101. Dragoman, D. and M. Dragoman, *Terahertz fields and applications.* Progress in Quantum Electronics, 2004. **28**(1): p. 1-66.

102. Nerkararyan, K., A. Hakhoumian, and A. Babayan, *Terahertz surface plasmon-polariton superfocusing in coaxial cone semiconductor structures.* Plasmonics, 2008. **3**(1): p. 27-31.

103. Keilmann, F., *Status of THz-to-visible nanospectroscopy development.* Journal of Biological Physics, 2003. **29**(2-3): p. 195-199.

104. Merlin, R., *Radiationless Electromagnetic interference: evanescent-field lenses and perfect focusing.* Science, 2007. **317**(5840): p. 927-929.

105. Ebbesen, T.W., et al., *Extraordinary optical transmission through sub-wavelength hole arrays.* Nature, 1998. **391**(6668): p. 667-669.

106. Bethe, H.A., *Theory of diffraction by small holes.* Physical Review, 1944. **66**(7-8): p. 163–182.

107. Martin-Moreno, L., et al., *Theory of extraordinary optical transmission through subwavelength hole arrays.* Physical Review Letters, 2001. **86**(6): p. 1114-1117.

108. Matsui, T., et al., *Transmission resonances through aperiodic arrays of subwavelength apertures.* Nature, 2007. **446**(7135): p. 517-521.

109. Cao, H. and A. Nahata, *Influence of aperture shape on the transmission properties of a periodic array of subwavelength apertures.* Opt. Express, 2004. **12**(16): p. 3664-3672.

110. Hendry, E., et al., *Ultrafast optical switching of the THz transmission through metallic subwavelength hole arrays.* Physical Review B (Condensed Matter and Materials Physics), 2007. **75**(23): p. 235305-5.

111. Hibbins, A.P., B.R. Evans, and J.R. Sambles, *Experimental verification of designer surface plasmons.* Science, 2005. **308**(5722): p. 670-672.

112. García de Abajo, F.J. and J.J. Sáenz, *Electromagnetic surface modes in structured perfect-conductor surfaces.* Physical Review Letters, 2005. **95**(23): p. 233901.

113. Zhichao, R. and Q. Min, *Slow electromagnetic wave guided in subwavelength region along one-dimensional periodically structured metal surface.* Applied Physics Letters, 2007. **90**(20): p. 201906.

114. Hendry, E., A.P. Hibbins, and J.R. Sambles, *Importance of diffraction in determining the dispersion of designer surface plasmons.* Physical Review B (Condensed Matter and Materials Physics), 2008. **78**(23): p. 235426-10.

115. Pendry, J.B., *Focus issue: Negative refraction and metamaterials - Introduction.* Optics Express, 2003. **11**(7): p. 639-639.

Appendix: Modes in a Coaxial Waveguide

The dispersion relation (3.24) can be represented as the quadratic equation with respect to $\xi = \frac{\varepsilon_d \kappa_m}{\varepsilon_m \kappa_d}$: $\alpha\xi^2 + \beta\xi + \gamma = 0$. Using this equation together with Eq. (3.24) yields to the following relations for coefficients α, β and γ:

$$\alpha = 1 - \frac{K_1(\kappa_d r)}{I_1(\kappa_d r)} \frac{I_1(\kappa_d R)}{K_1(\kappa_d R)}, \tag{A.1}$$

$$\beta = -\left(\frac{I_0(\kappa_d r)}{I_1(\kappa_d r)} \frac{I_1(\kappa_m r)}{I_0(\kappa_m r)} + \frac{K_0(\kappa_d R)}{K_1(\kappa_d R)} \frac{K_1(\kappa_m R)}{K_0(\kappa_m R)} \right) -$$

$$- \frac{K_1(\kappa_d r)}{I_1(\kappa_d r)} \frac{I_1(\kappa_d R)}{K_1(\kappa_d R)} \cdot \left(\frac{K_0(\kappa_d r)}{K_1(\kappa_d r)} \frac{I_1(\kappa_m r)}{I_0(\kappa_m r)} + \frac{I_0(\kappa_d R)}{I_1(\kappa_d R)} \frac{K_1(\kappa_m R)}{K_0(\kappa_m R)} \right),$$

$$\gamma = \frac{I_1(\kappa_m r)}{I_0(\kappa_m r)} \frac{K_1(\kappa_m R)}{K_0(\kappa_m R)} \left(\frac{I_0(\kappa_d r)}{I_1(\kappa_d r)} \frac{K_0(\kappa_d R)}{K_1(\kappa_d R)} - \frac{K_0(\kappa_d r)}{I_1(\kappa_d r)} \frac{K_1(\kappa_m R)}{K_1(\kappa_d R)} \right).$$

If the parameter $x = \kappa_d a$ where $a = R - r$ is small, i.e., $\kappa_d a << 1$ than these coefficients can be expanded over this parameter. Therefore, the general appearance of these coefficients is

$$\alpha = \alpha_1 x + \alpha_2 x^2, \tag{A.2}$$

$$\beta = \beta_0 + \beta_1 x + \beta_2 x^2,$$

$$\gamma = \gamma_1 x + \gamma_2 x^2.$$

Now let us substitute the coefficients in this form in dispersion relation for the even mode (3.25) (with minus sign), where $\beta / 2\alpha$ is expanding over x

$$\frac{\beta}{2\alpha} = \frac{\beta_0}{2\alpha_1 x} \left(1 + \left(\frac{\beta_1}{\beta_0} - \frac{\alpha_2}{\alpha_1} \right) x + \left(\frac{\alpha_2^2}{\alpha_1^2} - \frac{\alpha_2 \beta_1}{\alpha_1 \beta_0} + \frac{\beta_1}{\beta_0} \right) x^2 + O[x^3] \right), \tag{A.3}$$

while

$$\sqrt{\left(\frac{\beta}{2\alpha}\right)^2-\frac{\gamma}{\alpha}}=\left(\frac{\beta_0}{2\alpha_1}\right)\cdot\frac{1}{x}\cdot\frac{1}{\sqrt{1+2\left(\frac{\beta_1}{\beta_0}-\frac{\alpha_2}{\alpha_1}\right)x+\left[\left(\frac{\beta_1}{\beta_0}-\frac{\alpha_2}{\alpha_1}\right)^2+2\left(\frac{\alpha_2^2}{\alpha_1^2}-\frac{\alpha_2\beta_1}{\alpha_1\beta_0}+\frac{\beta_1}{\beta_0}\right)-\frac{4\alpha_1\gamma_1}{\beta_0^2}\right]x^2+O[x^3]}}. \tag{A.4}$$

Then for the sake of convenience, let us replace

$$A=\frac{\beta_0}{2\alpha_1},\quad \mathrm{B}=\left(\frac{\beta_1}{\beta_0}-\frac{\alpha_2}{\alpha_1}\right),\quad \mathrm{C}=\left(\frac{\alpha_2^2}{\alpha_1^2}-\frac{\alpha_2\beta_1}{\alpha_1\beta_0}+\frac{\beta_1}{\beta_0}\right),\quad \mathrm{D}=\frac{4\alpha_1\gamma_1}{\beta_0^2}. \tag{A.5}$$

The expansion of (A.4) into a Taylor series over the small parameter x leads to

$$\sqrt{\left(\frac{\beta}{2\alpha}\right)^2-\frac{\gamma}{\alpha}}=\frac{A}{x}\left(1+2Bx+\left[B^2+2C-D\right]x^2+O[x^3]\right)^{1/2}= \tag{A.6}$$
$$=\frac{A}{x}\left(1+Bx+\left[\frac{B^2+2C-D}{2}-\frac{B^2}{2}\right]x^2+O[x^3]\right)$$

Combining relations (A.3) and (A.6) and using notations (A.5), we obtain the mode equation (3.26)

$$-\xi=\frac{A}{x}\left(1+Bx+Cx^2+O[x^3]\right)-\frac{A}{x}\left(1+Bx+\left[C-\frac{D}{2}\right]x^2+O[x^3]\right)= \tag{A.7}$$
$$=\frac{AD}{2}x+O[x^2]=\frac{\gamma_1}{\beta_0}x+O[x^2]$$

where $\dfrac{\beta_0}{\gamma_1}=\dfrac{K_0(\kappa_m R)}{K_1(\kappa_m R)}+\dfrac{I_0(\kappa_m r)}{I_1(\kappa_m r)}$.